Alaska SAR Facility
Scientific SAR User's Guide

by

Coert Olmsted, Senior Programmer/Analyst

July 1993

ASF-SD-003

Scientific SAR User's Guide

TABLE OF CONTENTS

Preface

This document is intended to provide an introduction and background to scientists wishing to interpret SAR image data. The coverage is necessarily brief but thorough references and citations are provided for the user who wishes to pursue the subject in greater depth. An excellent general text, which should be on the shelf of any serious SAR investigator, is the recent (1991) book by Curlander and McDonough. For a good elementary exposition on the complexities of SAR signal processing see Fitch's 1988 book. Short courses on the subject are offered periodically at UCLA Extension, Department of Engineering, Information Systems and Technical Management, 10995 LeConte Avenue, Los Angeles, CA 90024-2883. Courses occur also at George Washington University, Continuing Engineering Education Program, Washington, DC 20052, and occasionally at the University of Alaska in Fairbanks.

For information on system details, accessing data and the user interface, the reader should obtain the *Alaska SAR Facility Archive and Catalog Subsystem User's Guide* [Desoto *et al.*, 1991] and the *Geophysical Processor System User's Guide* [Baltzer *et al.*, 1991] from the GeoData Center of the Alaska SAR Facility at the Geophysical Institute, University of Alaska, Fairbanks, AK 99775-0800, Rose Watabe, User Services Specialist (907) 474-7487. Other user's guides, listed in the Bibliography and References section, are also available.

Printing limitations prevent the use of any example images in this document. Remote sensing images are best presented in large format photographic prints and can be reproduced fairly well with an offset press. Photocopies, however, are largely useless so we have attempted to work around the need for such illustrations. For appropriate examples, particularly in Sections 3 and 4, we again recommend the book by Curlander and McDonough.

Coert Olmsted

Fairbanks, Alaska
April 1993

ACKNOWLEDGMENTS

The author thanks ASF Chief Scientist, Willy Weeks, and ASF Review Board member, Robert McDonough, for careful technical readings of the drafts of this document. Editorial assistance from Donna Sandberg and Debbie Ice is also gratefully acknowledged. The ASF support staff has provided valuable service in manuscript and document preparation.

The text has been produced mainly with *Lightning Textures*, a version of TEX for the Macintosh computer. Tables C1 and C2 were produced with *Microsoft Word*, the line graphs were produced with *Mathematica*, and the diagrams with *Adobe Illustrator*. Special thanks are due to Deborah Coccia for assistance with Figure 2.

All work has been performed under contract to the National Aeronautics and Space Administration (NASA).

Chapter 1
Imaging Radar

1.1 *INTRODUCTION*

Radar sensing has been developed on the basis of four technological principles. These are: 1) the ability of an antenna to emit a brief electromagnetic pulse in a precise direction, 2) the ability to detect, also with directional precision, the greatly attenuated echo scattered from a target, 3) the ability to measure the time delay between emission and detection and thus the range to the target, and 4) the ability to scan with the directional beam and so examine an extended area for targets. A fifth principle, spectral analysis of precisely phase controlled signals, enables extreme enhancements of the application of the four physical principals. It is this last methodology which lies at the heart of synthetic aperture radar (SAR). By means of detection of small Doppler shifts in signals from targets in motion relative to the radar, it is possible to obtain, from limited peak power, imaging resolutions on the order of 3 arc seconds for spaceborne SAR and 0.01 arc second for planetary radar telescopy. These techniques depend on precise determination of the relative position and velocity of the radar with respect to the target, and on integrating the return signal information over a time period (or *look*) which is long compared to the time between pulses (*inter-pulse period*, IPP).

1.2 *ANTENNA SIGNAL PROPERTIES*

From basic principles of electromagnetic optics we derive the directional pattern of transmission and reception of a radar antenna in terms of the Fourier transform of the signal current density throughout the antenna. A uniform density on a rectangular antenna (as in the case of Earth observing SAR) transforms to a sinc function (see Appendix A) the square of which gives the typical lobate pattern shown in Figure 1. The argument of the sinc^2 is the off mid-beam angle scaled by the size, D/λ, of the antenna in terms of the signal wavelength λ, so that solving for the angle within which a given power is attained (dotted lines in Figure 1), produces a value inversely proportional to D/λ. It turns out that the proportionality constant is near unity (.886), if the half power (3 dB) level is chosen and the beamwidth angle γ is expressed in radians. Thus $\gamma = \lambda/D$.

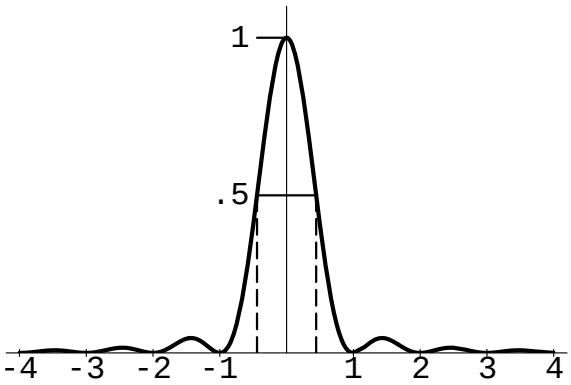

Figure 1. The sinc function squared with argument in units of λ/D.

This analysis is exactly the same as is used to derive the intensity pattern resulting from a point source of light illuminating a rectangular diffraction grating. Optical analogs are, in fact, very important in SAR processing and have been used to implement devices which produce the SAR image via Fresnel lensing of laser light through signal modulated film. Refer to Kovaly [1976, Ch. VI, p235].

For ERS-1, however, some phase shifting is introduced as the signal is applied across the width D of the antenna. The result is a broadening of the main lobe of

the directional pattern and a corresponding increase in the width of the beam in the range direction. The purpose is to get power distributed uniformly across the swath to a width of 100 km. In effect, it is preferred to have the beam spread out across the range (Figure 2).

Because of the symmetry between transmission and reception patterns, the same antenna is used for both functions, with a duplex switch gating between the high power output pulse and the low power returned echo signal.

1.3 *SCANNING CONFIGURATION*

To image terrain, the radar is carried on an aircraft or spacecraft platform moving at uniform speed and altitude. The forward motion provides scanning in the along track (*azimuth*) direction. The radar beam is directed to the side (most commonly perpendicular to the track, i.e., *squint angle* $= 0°$) and down toward the surface. The beam is wide in the vertical direction and so intersects the surface in an oval with the long axis extended in the across track (*range*) direction. The echo of a short pulse will be received from surface points at increasing range. Thus, digitizing the signal

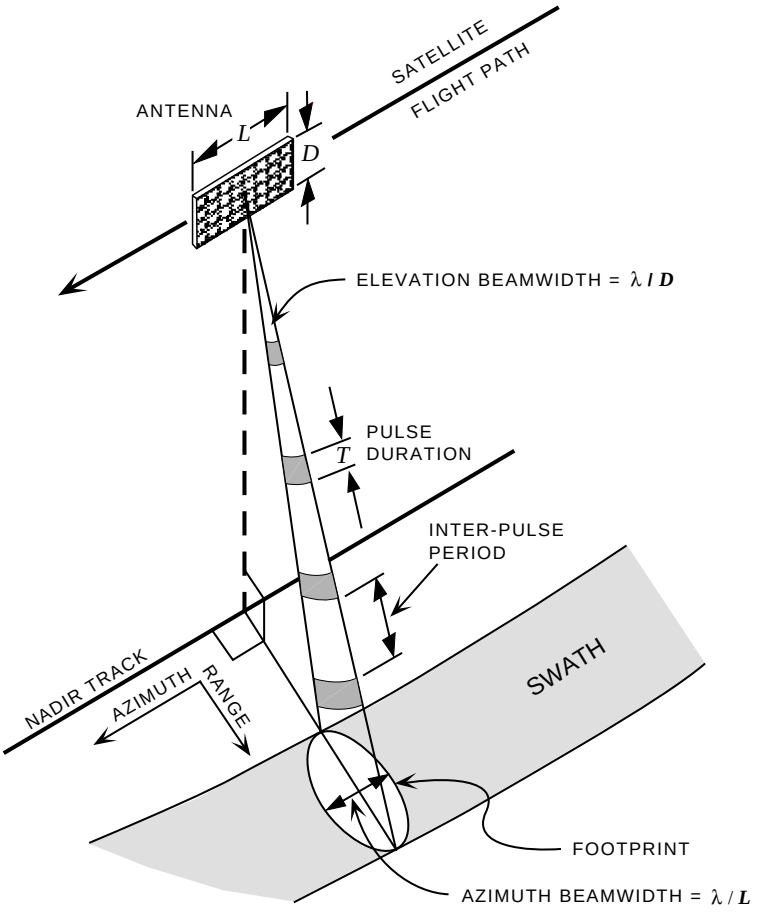

Figure 2. Scanning configuration for a left looking SAR with a rectangular antenna.

in time provides scanning in the range direction. This direction is determined by the side to which the radar looks. Side looking makes it unique as opposed to a nadir looking beam which would extend on either side of the nadir track. Then each travel time would correspond to a return from the right *and* the left side. For side looking, the general configuration is illustrated in Figure 2. Orbit characteristics and other information concerning this system are given in Table C1 of Appendix C.

Chapter 2
SAR Signal Processing Algorithms

2.1 *RANGE PROCESSING*

In the range direction a real aperture radar achieves resolution by emitting a brief intense rectangular pulse, then sampling the returned signal and averaging over time intervals no shorter than the emitted pulse. Each averaged value is then the backscattered intensity from the surface at the slant range corresponding to half the round trip travel time of the signal. Since the averaging interval is bounded below by the pulse length, the range resolution is directly proportional to the pulse length. High resolution requires short pulse length and, therefore, very high intensity levels in order to obtain adequate energy in the return signal for typical remote sensing satellite ranges. As a result the power requirements for orbiting SAR systems would appear to be excessively high.

Fortunately signal processing permits the use of an extended pulse at lower intensity, and thus lower power requirements, which will still emit enough energy to give a detectable return. Although the returns from points at adjacent range intervals overlap in time, the shape of the pulse is distinctive enough for signal analysis to enable the components of the superimposed signals to be resolved. In effect, a matched filter for the emitted pulse will recognize the elements of the distinctive signal and delay them successively so that they are all compressed into a short spike with intensity proportional to that of the extended echo.

2.1.1 *Matched Filtering*

In the following sections we discuss signals f, g, s as complex valued functions of a real time variable t. The complex conjugate of f is denoted f^* and its modulus or absolute value by $|f|$. The symbol ':=' means 'equal by definition' and defines the object on the left to be the expression on the right.

There are a number of ways to implement a matched filter. The easiest to visualize is the technique of correlation. The autocorrelation of a signal is defined as a function of lag (or time delay). For a given lag, τ, the signal, f is advanced by that amount, multiplied by its complex conjugate and the product averaged over the signal length,

$$\mathrm{acf}_f(\tau) := \int_{-\infty}^{\infty} f^*(t) f(t+\tau)\, dt. \tag{1}$$

If, without loss of generality, the signal is referred to its mean, it will fluctuate around zero. At zero lag the integrand will be the magnitude squared and the integral will represent the energy $E_f = \int_{-\infty}^{\infty} |f(t)|^2\, dt$, a positive quantity. If the signal shape changes with time, then it is unlike itself when delayed and the values of the integrand will have essentially random positive and negative values which will tend to cancel out when integrated. Thus the autocorrelation function will have low magnitude for large lags, i.e., the signal is uncorrelated with itself when delayed. In any case the Schwartz inequality gives $|\mathrm{acf}_f| \leq E_f$ at all lags.

The object then in designing a distinctive signal is to choose one with a very narrow autocorrelation function. Then when the returned echo is correlated with the known transmitted signal, a narrow pulse will result at the lag corresponding to the round trip travel time. Thus we match the echo to the original pulse at the delay appropriate to the range of the target. It is this method which leads to the use of the term *correlator* to refer to a digital SAR processor. Although, as we shall see, the processing may not be a direct correlation, it is always mathematically equivalent.

One such pulse shape, which is uncorrelated at large lags, is given by a harmonic, the frequency of which increases linearly with time. This is called *linear frequency modulation* (FM) and, when of limited duration, produces a chirp, if considered in the auditory frequency range. An infinite chirp such as $\sin t^2$ has, in fact, an autocorrelation function which is zero everywhere except at zero lag. A finite chirp modulating carrier frequency f_0, of length T and chirp frequency rate a is

$$f(t) = e^{i2\pi(f_0 t + .5at^2)}, \quad 0 \le t \le T, \tag{2}$$

which has a much more complicated autocorrelation function that, nevertheless, can be calculated explicitly [Fitch, 1990, p8] as

$$\mathrm{acf}_f(\tau) = \Phi(\tau) \cdot (T - |\tau|) \cdot \frac{\sin\left(\pi a \tau (T - |\tau|)\right)}{\pi a \tau (T - |\tau|)}. \tag{3}$$

Here Φ is the carrier harmonic which is modulated by a triangle pulse and a sinc of quadratic time. In Figure 3, which shows the shape of the envelope, it is clear that the chirp has been compressed into a narrow spike. The first root of the sinc occurs when the argument of the sin is π, which is approximately at $\tau = 1/aT$. Thus the main lobe width is $2/aT$ and the half power width is about $1/aT$.

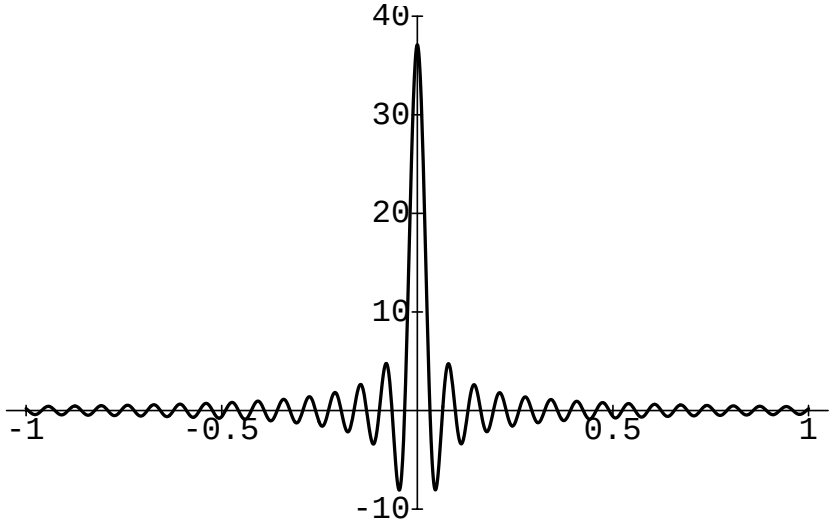

Figure 3. Chirp autocorrelation function. The time units are microseconds and the vertical axis is correlation in energy units (watt-microseconds).

The frequency of the chirp is the first time derivative of the phase in Equation (2), i.e., $2\pi(f_0 + at)$, so that the bandwidth is clearly aT over the pulse duration T. The gain in resolution, or *pulse compression ratio*, is T divided by $1/aT$ or aT^2. This is also the time-bandwidth product of the chirp signal. Thus for high resolution we want a high time-bandwidth signal. Such signals are also called *sophisticated* because of their ability to carry more information. For a theoretical (and sophisticated) treatment see Vakman [1968]. High time-bandwidth implies a large chirp rate, a, since the pulse duration, T, is constrained by a number of considerations, particularly the need to receive over an extended interval in order to image a wide swath on the surface. This is because the single antenna cannot receive and transmit at the same time, so transmit time must be a small fraction of the IPP. Using parameter values for the ERS-1 SAR instrument (as we shall do throughout this document in numerical examples) we have $T = 37.1$ μsec and the bandwidth a is 15.5 MHz, so $aT^2 = 575$. The Bandwidth Theorem puts a theoretical lower bound of 1 on the time-bandwidth product of any signal (the minimum being realized only by a Gaussian pulse). Thus the ERS-1 chirp is highly sophisticated by more than 2 orders of magnitude.

Mathematically a filter operation is expressed as convolution of the input f with an impulse response function h, giving output

$$g(\tau) = f * h := \int_{-\infty}^{\infty} f(t)h(\tau - t)\, dt. \tag{4}$$

Here '$*$' denotes the convolution operator defined by (4). To make convolution look like autocorrelation, choose $h(t) = f^*(-t)$. Then

$$\begin{aligned} g(\tau) &= \int_{-\infty}^{\infty} f(t)f^*(t - \tau)\, dt \\ &= \int_{-\infty}^{\infty} f(t' + \tau)f^*(t')\, dt' \\ &= \mathrm{acf}_f(\tau). \end{aligned} \tag{5}$$

The second integral is obtained by the change of variable $t' = t - \tau$. Thus autocorrelation amounts to convolution, i.e., (matched) filtering with the time reversed complex congugate of the original signal.

In essence matched filtering seeks an approximate solution for the convolutive inverse of the input signal. That is, we want to solve for h in $f * h = \delta$, where δ is the Dirac delta function, a unit impulse at time zero (more generally, $\delta(t - t_0)$ is the unit impulse at time t_0). Delta functions are a convenient abstraction representing the limit of functions such as (3) (Figure 3) as the lobe width tends to zero. A major virtue of the delta function is its *sifting* (or convolutive identity) property whereby

$$f * \delta = \int_{-\infty}^{\infty} f(t)\delta(\tau - t)\, dt = f(\tau), \tag{6}$$

i.e., the delta function extracts the value of a signal at a specific time. This is the reason the function h characterizing a filter in (4) is called the *impulse response function*. If the filter is probed with a delta impulse for input, the output (response) will be h.

Now let the pulse $f(t)$ be transmitted and the return signal be sampled (digitized) at intervals Δt. If $N+1$ evenly spaced samples are taken, the measured response at the antenna will be

$$s(t) = \sum_{i=0}^{N} \alpha_i f(t - i\Delta t), \tag{7}$$

where α_i is the level of scattering from the range corresponding to sample time $i\Delta t$ and the terms will be superposed in the general case that $\Delta t < T$. Now convolve this with the inverse pulse h as in (5). Approximating the normalized acf_f with δ, the output is

$$\begin{aligned} g := h * s = \sum_{i=0}^{N} \alpha_i h * f(t - i\Delta t) &= \sum \alpha_i \mathrm{acf}_f(t - i\Delta t) \\ &\approx \sum_{i=0}^{N} \alpha_i \delta(t - i\Delta t). \end{aligned} \tag{8}$$

Thus, using the discrete version of the sifting property, g is a discrete time series with values α_i,

$$g_i := g(i\Delta t) = \alpha_i, \qquad i = 0, 1, \ldots N, \tag{9}$$

which is just the appropriate form to represent an image line.

2.1.2 *Reference Function and Windowing*

Numerically convolution is very computation intensive. For efficient calculation of g it is more practical to Fourier transform the data to the frequency domain where, by the Convolution Theorem, convolution corresponds to multiplication and conversely:

$$\mathcal{F}\{h * f\} = \mathcal{F}\{h\}\mathcal{F}\{f\}. \tag{10}$$

The transformed impulse response function, $\mathcal{F}\{h\}$, known as the *frequency response function*, can be computed [Fitch, 1990, p. 10] as

$$\mathcal{F}\{f^*(-t)\} = (\mathcal{F}\{f\})^*, \tag{11}$$

the complex conjugate of the pulse transform. In SAR processing it is known as the *reference function* and also has the form of a chirp since the transform of a (complex) Gaussian is again a Gaussian (Appendix A). The Fourier transforms for discrete data can be done efficiently by the Fast Fourier Transform (FFT) algorithm and its inverse (FFT^{-1}). Thus the filtering operation is composed of a forward FFT, multiplication by the reference function, followed by inverse FFT.

The output of the chirp matched filter shown in Figure 3 is the ideal response of the signal correlator to the return from a point source. Clearly the resolving capability

of the system is determined by the narrowness of the main lobe and its separation from, and amplitude ratio to, the sidelobes. For ERS-1 range processing, the width is about 0.13 μsec, the separation of the first sidelobe is about 0.10 μsec, and its relative amplitude is about 0.21. Since the range sampling rate is 18.96 MHz, the sampling interval is about 0.053 μsec which is about half the lobe separation. This implies that successive compressed pulses will have sidelobe overlap and a significant amount of the image intensity will be ambiguous between a pixel and its neighbors.

This analysis is an example of the use of the *ambiguity function*, a generalized autocorrelation of the signal waveform, which measures the success of pulse compression in terms of its ability to provide target resolution [Vakman, 1968, §8].

To compensate for this sidelobe ambiguity, it is useful to weight (or *window*) the returned signal over the integration time. Equivalently, the windowing can be done in the frequency domain where it can be efficiently incorporated into the reference function. The result of this signal modification is a reduction of the sidelobe amplitude at the cost of widening the main lobe of the compressed pulse output. For a fixed level of sidelobe reduction, the weighting function can be determined as the solution of an optimization problem which minimizes the main lobe width. The result, after a number of approximations [Curlander and McDonough, 1991, Ch. 3.2.3], is a window function of the *cosine on a pedestal* form, $W(f) = \alpha + \beta\cos(2\pi f/B)$, where B is bandwidth and $\alpha + \beta = 1$. The most widely used such function is the *Hamming window* for which $\alpha = .54$.

2.2 *AZIMUTH PROCESSING*

Real aperture radar achieves azimuth (along track) resolution by means of a tight beamwidth. This requires a large antenna since beamwidth is inversely proportional to antenna size and directly to signal carrier wavelength. For ERS-1 the beamwidth is about .3° which, although small, nevertheless gives a footprint on the earth's surface of about 5 km. At a pulse repetition frequency (PRF) of 1680 Hz, the beam footprint moves only 4 m between pulses. Thus although azimuth information is sampled at very high resolution, the echo signal from a target is distributed over a large number of samples corresponding to the along track spatial extent. It is also superposed on similar sample clusters from adjacent target locations so that, as in the range case, signal processing is needed to integrate this data into a compressed pulse attributable to a compact target.

2.2.1 *Doppler Variation and Pulse Compression*

The problem then is to distinguish the echo signal in terms of its position within the beam, i.e., to find its variation with time during the interval that the beam sweeps past the target. This interval is known as the *coherent integration time*.

A signal received at a moving antenna will be altered in frequency according to the well known Doppler shift. See Appendix B for a discussion of this phenomenon. The frequency shift f_D will be proportional to the relative speed of source and receiver,

$$f_D = -\frac{2}{\lambda}\frac{dR}{dt}, \tag{12}$$

where λ is transmitted wavelength and R is the slant range distance from target to antenna. As in Figure 4, let the spacecraft pass the target at closest approach at time $t = 0$ and slant range R_0 which is perpendicular to the track. If the spacecraft has orbital speed V, then, neglecting earth rotation, the Pythagorean formula gives

$$R^2 = R_0^2 + (Vt)^2. \tag{13}$$

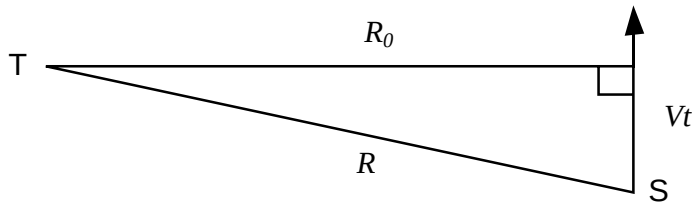

Figure 4. Geometry to compute the relative velocity of the spacecraft, S, and the target, T, in order to estimate the Doppler shift as a function of time, *t*. The spacecraft velocity is *V*.

Differentiate (13) with respect to t to obtain

$$\begin{aligned} 2R\frac{dR}{dt} &= 2V^2 t \\ \frac{dR}{dt} &= \frac{V^2}{R}t. \end{aligned} \tag{14}$$

This is an approximation in that the orbit path is not a straight line. The error is on the order of the small angle approximation for an angle of about

$$\text{(5km footprint)/(7150km orbit radius)} < .0007\text{radian},$$

which implies an error of less than 1 in 10^7.

Thus, to high precision, the Doppler frequency variation of the signal is

$$f = f_0 + f_D = f_0 - \frac{2}{\lambda}\frac{V^2}{R}t, \tag{15}$$

i.e., linear FM. Since the footprint is also fairly small compared to slant range (Formula (16) below), R is relatively constant so that, as the azimuth varies, the returned signal will be sampled at about the same place in the chirp pulse. Thus at fixed range the phase of the signal due to the chirp waveform will be constant along the azimuth sampling at the PRF. Therefore, to the extent that V^2/R is time independent, the signal variation with azimuth is a chirp. Thus the same pulse compression technique as for the range processing can be used. Note that the factor V^2/R is the centripetal acceleration of the spacecraft with respect to the target as long as R is close to R_0. Using the ERS-1 footprint of 5km and minimum slant range of $R_0 = 845$km we have

$$1 \le \frac{R}{R_0} \le \sqrt{1 + (5/R_0)^2} = 1.000018 \tag{16}$$

so that R varies from R_0 by at most 2 parts in 10^5. We have also made an approximation by assuming that the signal wavelength λ in (12) is constant. But, in fact, the frequency of the signal varies (linearly) over the chirp bandwidth of 15.5 MHz. This may seem a lot, but compared to the frequency, 5300 MHz, of the carrier wave the error is about 3 parts in 1000 which is the largest error of approximation. In practice the use of a chirp matched filter for azimuth SAR processing gives excellent results.

Chapter 3
Accuracy and Geometric Distortion/Correction

3.1 *RESOLUTION*

From our discussion of signal processing in Section 2, we see that to associate a scattering intensity to a specific location within an image requires signal processing of the extended returned pulse. This compresses it into a brief duration and so localizes its source. Thus the fineness of the spatial resolution in the derived image depends on the accuracy with which we can perform this signal processing.

There are a number of phenomena contributing errors to the signal processing, but a surprising and important fact is that the range (radar to target distance) is not a direct factor affecting resolution. Theoretically, the resolving power of a SAR instrument is independent of its altitude. This can be shown as follows: Our basic result from Section 1 is that angular beamwidth γ (radians) is inversly proportional to antenna size L and directly to signal wavelength λ,

$$\gamma = \lambda / L \tag{17}$$

Thus the footprint L_{eff} of this beam at range R is

$$L_{\text{eff}} = \gamma R = \lambda R / L \tag{18}$$

and this length measures the amount of terrain illuminated by the chirp pulse. The conceptual breakthrough made by the early researchers in this field was to realize that the length L_{eff} represents the *effective* aperture of the moving radar. It is the distance travelled by the antenna while the target is within the beam, so that all pulses emitted during this time (about 1000 for ERS-1) contribute some information about the target backscatter. Thus the amount of information that can be unravelled by signal processing is directly proportional to this effective length. Physically, it is equivalent to emitting a single pulse and receiving a point target echo over a 1000 antenna array of this length (about 4km for ERS-1) for which the phase has been corrected at each antenna by the delay due to the round trip travel time. Collecting phase shifts for the round trip effectively doubles the array length so that applying Formula (17) to get the effective beamwidth gives

$$\gamma_{\text{eff}} = \lambda / 2L_{\text{eff}}. \tag{19}$$

Now we can calculate the azimuth resolution ρ_z as the effective footprint of the effective beamwidth intercepting the terrain at range R which is, using Equation (18),

$$\rho_z = \gamma_{\text{eff}} R = \frac{\lambda R}{2L_{\text{eff}}} = \frac{\lambda R}{2\frac{\lambda R}{L}} = \frac{L}{2}. \tag{20}$$

Thus theoretical resolution (assuming perfect signal processing) depends only on physical antenna size L and is finer for smaller antennas.

Cutrona [Skolnik, 1990, p21.3] characterizes this discovery as "spectacular" and highly motivating for him and the team which developed the first airborne SAR at the University of Michigan in the middle 1950's.

Another application benefitting from this kind of spectacular resolution is the imaging of Venus from Earth with the Arecibo (Puerto Rico) radar ($\lambda = 70$ cm) using a SAR-like technique known as delay-Doppler [Walker, 1980]. Signal processing of phase encoded pulses enables discrimination of differential travel time delay and Doppler shift due to Earth-Venus relative motion which, when integrated over 2.5 hours of pulsed signal transmission gives subkilometer resolution at a range of over 40 million kilometers. This is angular resolution on the order of 5×10^{-3} arc seconds — an improvement of 5 orders of magnitude over the real aperture resolution available at 70 cm wavelength from a 305F m antenna.

In Section 2.1.1 we saw how the sophistication (or high time-bandwidth product) of a signal contributes to the resolvability of a target in the image. For azimuth processing the duration of the signal is the coherent integration time (footprint length/swath velocity) $= R\lambda/LV$ and the bandwidth is this time multiplied by the Doppler rate $f_R := \dot{f}_D$. Employing the usual model from (15) of $f_R = 2V^2/\lambda R$ we then obtain for the time-bandwidth product the expression $2\lambda R/L^2$. For ERS-1 this has the value 957 so that the azimuth chirp is quite as sophisticated as the range chirp and resolution is not limited by signal processing parameters.

One might hope to optimize resolution with a very small antenna. However, other aspects of the imaging process depend on the antenna size. In particular, swath width, pulse length, antenna size and PRF are subject to mutual constraints in order to achieve appropriate image size and to avoid range ambiguities due to multiple pulses arriving during the IPP. See Elachi *et al.* [1982, II.A] for an analysis that puts a lower limit on antenna size.

3.2 *PROCESSING ERRORS*

In order to correlate the returned signal precisely throughout the coherent integration time or, equivalently, to adjust the phase for the various slant range travel times, it is necessary to have precise timing. This is accomplished with a stable local oscillator (STALO) which drives the signal at sub-microsecond accuracies and is able to maintain phase to within $\pi/4$ or one eighth cycle.

However, in Section 2 a number of approximations and simplifying assumptions were introduced. These make the formulas used in signal processing geometrically inexact and so require corrections, usually to the pixel locations of the processed data. One such resampling requirement is to obtain uniform ground range sample spacing. By digitizing uniformly in time (at 18.96 MHz), the samples are uniformly spaced in slant range at about 7.9 m, which implies ground range spacing that varies from 24 m to 18 m with increasing range. Thus the nominal 12.5 m range pixel size represents an interpolated resampling.

3.2.1 *Relative Motion and Doppler Estimation*

In Appendix A we show how the reference function is computed from the base frequency and the chirp rate. For range processing, these parameters are known from the

outgoing signal characteristics. For azimuth processing they must be determined from the Doppler shift f_D and its rate of change f_R (together known as *Doppler history*). The relevant parameter for azimuth processing is the Doppler shift at the moment the beam center crosses the target. This is known as the Doppler *centroid*. Appendix B shows how the Doppler shift depends on relative spacecraft to target velocity. If this information can be obtained precisely, in a common coordinate system, from spacecraft ephemeris (tracking data) and earth motion, then Doppler shift and rate can be calculated with comparable precision. The relative velocity can be significantly perturbed, however, by spacecraft attitude changes which affect the beam direction. These motions (roll, pitch and yaw) are not as easily or as precisely determined, as they must be measured by on-board sensors. Also, estimating the target location from the intersection of beam center with the earth surface is affected by the imprecision of the beam geometry. In fact, as shown in Section 4.1.1, the best method for obtaining the target location (i.e., pixel position on the earth surface) uses f_D as a known parameter.

Because SAR azimuth signals are highly sophisticated (Section 3.1), the principle of stationary phase can be used to deduce a direct relationship between signal frequency and azimuth position. Appendix A (Section A2) shows how errors in f_D can be corrected geometrically.

3.2.2 *Clutterlock and Autofocus*

Failing prior knowledge of Doppler parameters, the values can be estimated directly from the image data itself. A preliminary guess for the parameter is used to process the image, then the quality of the image is evaluated quantitativly with respect to the parameter and a best estimate computed to optimize image quality. Thus the Doppler centroid is estimated as the mode of the azimuth (Doppler) spectrum which is computed from echoes from a homogeneous target. This is called *clutterlock* since it homes in on the Doppler null for a uniform background return signal. Such signals are historically known as *clutter* which surrounds the target blip, particularly in marine applications where scatter from the rough sea surface generates a randomly noisy background. Thus ocean scenes are optimal for the clutterlock technique.

As noted in Equation (15) the frequency varies linearly with time so that the spectrum may be obtained by dividing the coherent integration time into sequential subintervals and computing the energy returned during each interval. These data segments represent the application of the pulse compression processing over only a part of the synthetic aperture and are referred to as *looks*. For purposes which will be explained later in the discussion of speckle, it is useful to divide the processing into 4 equal looks. This produces 4 subintervals of the Doppler spectrum. The center frequency is chosen so as to balance the energy in looks 1 and 2 with the energy in looks 3 and 4. This frequency is then the best estimate of the Doppler centroid.

If the Doppler centroid can be computed from relative motion data, then the Doppler rate can be computed by differentiation. If, however, the relative motion information is not reliable, a data dependent method must be used to obtain this parameter. The technique, known as *autofocus*, depends on the fact that echo data processed at an erroneous Doppler rate will be misregistered in azimuth between different looks. Thus

the resulting image will be blurred or apparently out of focus. If separate looks are cross correlated line by line, the misregistration will result in lower correlation values for improper Doppler rates. The rate which maximizes the cross correlation between looks can then be selected as a best estimate.

As in matched filtering, correlation variation is enhanced by a distinctive, nonuniform signal. Thus inhomogeneous scenes are best for autofocus in conflict with the requirements for clutterlock. Empirically it is found that urban scenes are a reasonable compromise between the two. Alternatively, separate parts of a scene, each having appropriate characteristics, may be used for the two techniques.

In practice, the Alaska SAR Processor (ASP) uses clutterlock to get f_D. Then, using the methods described in Chapter 4, it computes the target location $\mathbf{R}_{\mathrm{T}}$ from f_D and other information. From this, relative sensor-target velocity can be computed and, by differencing, the second derivative of R to obtain finally the Doppler rate,

$$f_R := -\frac{2}{\lambda}\frac{d^2R}{dt^2}. \tag{21}$$

3.2.3 *Ambiguity*

Since SAR processing uses discrete signal analysis, the extent of the Doppler spectrum is limited by the sampling rate according to the well known Nyquist frequency theorem [Curlander and McDonough, 1991, Appendix A.2]. Signal power at greater frequencies will be folded into the spectrum as multiples of the base freqency (i.e., *aliased*). For azimuth processing, azimuth location is related to Doppler frequency. The sidelobes of the antenna pattern (Figure 1) may pick up target energy outside the footprint, i.e., at multiples of the Doppler spectral limit (which is the PRF). The energy in these echos will be considerably lower than that from the mainlobe. However, in cases where a very bright target appears at an azimuth displacement corresponding to a multiple of the PRF, and the mainlobe target is uniform and dim, the bright target can appear superimposed over the dim one. Thus, bright parts of the image can be repeated at diminished intensity (*ghosts*) in the azimuth direction at intervals corresponding to multiples of the PRF.

Appendix A, Section A2 gives formulas relating the frequency error to the distance displacement. For the first ambiguity multiple Δf=PRF=1680 Hz for ERS-1, and the displacement is about 6 km. Thus there are opportunities for ghosts in images with brightness contrasts on these distance scales. Lacking brightness contrasts, these ambiguities will contribute to the background noise. A similar analysis shows that the range ambiguities occur at distances which are more on the order of the pixel size. Thus ghosts are less likely in range processing.

3.2.4 *Range Migration*

Although Equation (16) shows that the variation in range is small during the azimuth integration time, it is large enough to shift the target one or more pixels in the range direction, i.e., the lines of equidistance from the target are circles and so not coincident with the straight flight track on the surface. From (16) the maximum of

$R - R_0$ is about 15 m, so the maximum shift is on the order of 2 pixels in slant range. This is called *range curvature*.

A larger shift in apparent range is due to the rotation of the earth. Our simplified analysis of azimuth processing assumed the target-spacecraft relative motion to be along the spacecraft track. The direction of the swath velocity with respect to the earth surface varies significantly from east-west at the most polar extent of the orbit, to about 8.5° off north-south at the equator crossings. Half of the passes of the satellite over a given location on the earth will be *ascending* (i.e., north trending) while the other half, known as *descending*, will be travelling in the opposite direction. The surface component of the earth rotation is an eastward vector with magnitude $v_e = \omega_e R_e \cos\zeta$ where $\omega_e = 7.229 \times 10^{-5}$ rad/sec is the earth's sidereal angular speed and R_e is the earth radius which depends on latitude ζ. This is approximately $v_e = 0.46 \cos\zeta$ km/sec. For ERS-1 at the most northern extent $\zeta = 84.58°$ and $v_e = 0.0434$ km/sec either parallel or anti-parallel to the swath velocity. At the equator $v_e = 0.46$ km/sec is at an angle of either 98.52° or 81.48° to the swath track depending on whether the pass is ascending or descending.

However the earth rotation component adds to the swath velocity, it creates a shift in the relative motion of SAR and target. This shift in relative velocity causes a corresponding change in the direction of the Doppler centroid. The resulting displacement of data in the range direction is called *range walk*. In fact, any deviation of the system, such as beam pointing away from broadside (squint) or Doppler centroid error, will contribute to range walk and result in a skew of the processed image. Post processing corrects this with a *deskew* resampling procedure.

Together these range displacements are called *range migration*. The processing algorithm compensates for them by resampling along a curved path in the raw range-azimuth plane. This path is computed from geometric parameters which determine the precise relative motion of SAR and target.

3.3 *MISCELLANEOUS GEOMETRIC ERRORS*

The assumption of constant spacecraft altitude is not exact. The geoid is eccentric as is the spacecraft orbit. The first amounts to a variation of about 21 km between pole and equator while the latter is only a few meters at most. Terrain variations are on the order of a few kilometers. The effect of this altitude variation on the relative motion of target and spacecraft is accounted for by the relative motion algorithms as discussed in the previous section. Terrain variation will be discussed in the next chapter. The satellite altitude variation of about 100 m during an image skews the range and azimuth lines away from rectangular. Interpolation and resampling correct these effects so that the scale error is on the order of 0.1% [Bicknell, 1992, Ch. 3.3-4]. The orbit eccentricity also induces some spacecraft orbital velocity variation which will influence the line spacing since the PRF is constant. For ERS-1 $e = 1.165 \times 10^{-3}$ which implies a velocity variation over a semi-period of no more than 0.23%. This spans about 200 scenes so that the scale variation within one scene is neglible.

Azimuth pixel spacing can also vary with range due to the fact that earth rotation, and therefore swath speed, varies with latitude. In the worst case, near the poles, the error is still less than 0.1% or 100 m over a 100 km swath.

Another possible perturbation of the relative motion, and therefore the Doppler parameters, could be induced by local motions of the target such as water waves, swaying vegetation, drifting flotsam, or moving vehicles. These are unusual and must be accounted for on a case-by-case basis. In some instances, such as regular ocean waves over a large area, information about the surface phenomenon can be deduced from its effect on the SAR image [Ulaby *et al.*, 1986, Ch. 20-3].

3.4 *ATTENUATION AND NOISE*

3.4.1 *The Radar Equation*

There are many factors affecting the power that is returned to a SAR from a target and finally plotted as a pixel intensity in an image. Considerations such as transmitted power, spherical spreading, antenna gain, signal wavelength, PRF, pulse compression, receiver noise and bandwidth, target resolution and scattering cross section, and aperture synthesis are discussed in detail in Skolnik [1990, Ch. 21.16] and Curlander and McDonough [1991, Ch. 2.8]. These authors derive an expression for the signal to noise ratio (SNR) of the return for a distributed target which can be abreviated as

$$\mathrm{SNR} = A\frac{\overline{P}\sigma^0\rho_r}{R^3\lambda V}, \tag{22}$$

where A is a collection of factors depending on the antenna geometry and receiver thermal noise. For a given SAR instrument these are fixed. Other quantities depend on the transmitter (average power $\overline{P}$ and signal wavelength λ), the orbit (slant range R and spacecraft velocity V), signal processing (ground range resolution ρ_r), and the target (backscatter coefficient σ^0).

Non-obvious conclusions are that the power falls off as the cube of the distance and is inversely proportional to signal wavelength and spacecraft velocity. On the other hand, effective signal processing increases resolution, and therefore, echo detectability. The backscatter coefficient σ^0 is characteristic of the material and state of the target and is, therefore, of primary concern. It is a fundamental parameter of the image data and is related to the radar scattering cross section σ as the reflectivity per unit area, $\sigma = \sigma^0\rho_z\rho_r$.

3.4.2 *Speckle and Multilook Processing*

For a remote sensing imaging radar, the size of a resolution cell on the surface is always much larger than the signal wavelength and is generally significantly larger than the size of the individual scattering objects. Because of the commonly random orientation of terrain surface elements, returns from multiple scatterers within a resolution cell add incoherently to give a net backscattering coefficient which has a random distribution in the image plane. This variation (known as *speckle)* is independent for

distance scales larger than the effective beam footprint. Using (20), this has a size (for ERS-1) of

$$\frac{\lambda}{L}R = \frac{\lambda R}{2\rho_z} = 1.9 \text{ km}. \tag{23}$$

Statistical estimates of σ^0 can be improved by averaging over spatial scales larger than this, necessarily degrading spatial resolution.

Alternatively, the averaging can be done in the processing stage over the multiple looks which were discussed in the section on clutterlock and autofocus. Because of computational efficiencies and favorable statistics, as well as auxiliary uses for multiple looks, multilook averaging is the preferred method for reducing speckle noise. Since, however, each look uses a reduced synthetic aperture, the spatial resolution, being inversely proportional to Doppler bandwidth, is correspondingly reduced.

Signals added incoherently (random phase) sum in amplitude like a random walk. In the spatial coordinates this leads to an exponential distribution of detected power. When pixel values are averaged over a number of looks, the standard deviation of the estimate of σ^0 is reduced by the square root of the number of looks and the resulting spatial distribution becomes χ^2.

3.4.3 *Thermal Noise*

Such background noise occurs in all electronic systems, is usually Gaussian in time, and adds a bias to the image intensity. Thus, calibrating the noise power of the receiver in the absence of data signal, permits the bias to be removed. The noise variance, however, will still degrade the image SNR to something less than the square root of the number of looks.

3.4.4 *Radiometric Calibration*

From the radar equation it can be seen that the signal intensity has a strong dependence on range. Other factors influencing the signal level which also vary with range are incidence angle and antenna gain pattern. In addition, receiver noise and other system gains/losses must be taken into account. Internal instrument calibration is performed as an engineering task. External calibration for end-to-end ground truth evaluation of the entire system can be done by measuring the response to known point targets on the ground. Aluminum trihedral *corner reflectors* of known size, shape, orientation and radar cross section have been placed at strategic locations in the station mask for this purpose.

The final result of these calibration procedures is a function giving the correction to pixel intensity as a function of range (cross track pixel number). The function values are supplied as an array in the header records of the image file and are applied to the image data as part of the post processing. See Bicknell [1992, Ch. 3.6] for details.

Chapter 4
Geometric and Geographic Calibration and Registration

4.1 *GEOGRAPHIC PIXEL LOCATION*

The image product from a SAR, as in other imaging remote sensors, is a picture of the surface which, once corrected for geometric errors, can be regarded as a map with relatively high resolution and scale accuracy. A significant difficulty, however, for interpretation lies in *geolocation*, i.e., determining the overall location of the image in geographic (latitude, longitude) coordinates. While the satellite position and velocity can be determined to very high accuracy, its attitude is measurable to lower precision and controllable/predictable to an even lesser extent. Even small pointing errors will, at typical remote sensing distances, result in large displacements on the surface. For ERS-1 a yaw of well under 0.1° can result in a ground location error on the order of 1 km.

For optical and other passive radiometric sensors, the most effective method of geolocation is *tiepointing* in which known geographic features are matched between the image and map data derived by conventional methods. This, of course, works only for previously mapped regions. Oceanic scenes (particularly sea ice), remote or cloud obscured interior land areas without distinguishing features, and extraterrestrial surfaces cannot be so geolocated.

4.1.1 *Location Equations*

SAR, however, being an active radar instrument, provides very accurate information on the range to the target and the Doppler history of the returned signal. Because these quantities can be related to the precise spacecraft and earth surface coordinates, it is possible to solve a set of equations giving the earth location for each image pixel to an accuracy on the order of 100 m.

Referring to Figure 5, consider a geocentric Cartesian coordinate system oriented to the sun-earth orbit so that the x-axis points to the *vernal equinox*. This is an earth-sun direction at the time when the earth's axis is perpendicular to the earth-sun line. It occurs twice a year and marks the occasion of equal periods of night and day. On the spring (vernal) occurrence, the relative motion of the sun with respect to earth is south to north. The z-axis coincides with axis of rotation and is positive to the north. The y-axis completes a right-hand rectangular system so that the xy-plane coincides with the earth's equatorial plane. This coordinate system is known as *geocentric equatorial inertial* (GEI) and is used universally for tracking objects in local earth orbit. The vernal equinox is in the general direction of the constellation Aries, hence its ram symbol Υ. Small perturbations of the earth's rotational axis with respect to the ecliptic result in a slow migration of the vernal equinox with respect to the fixed, i.e., astronomically least mobile, stars. However, for our time scales, the physics of the coordinate system can be regarded as fixed inertial.

In this reference frame, the rotation of the earth has a period of one sidereal day, $P_\oplus = 23.93447$ hr, implying a rotational velocity vector of $\overrightarrow{\omega_e} = (0, 0, \omega_e)^T$, where $\omega_e = 7.2292115 \times 10^{-5}$ rad/sec. The coordinates of a point fixed on the earth (a target)

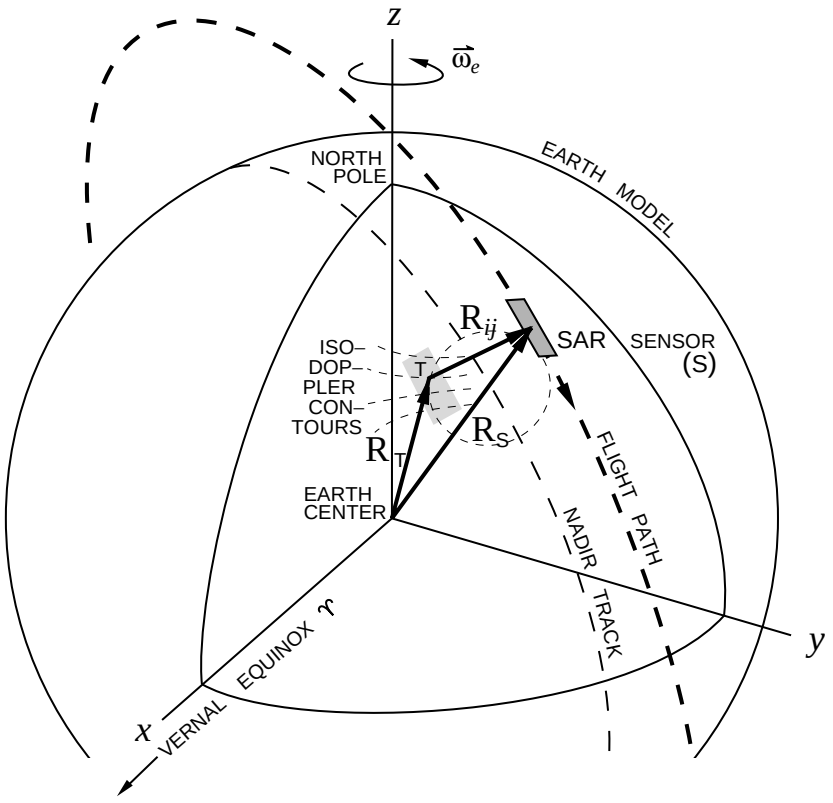

Figure 5. Earth model with GEI coordinate system and spacecraft and target position vectors. The geolocation procedure intersects $\mathbf{R}_{ij}$ with the rotating earth model surface (dashed circle) and the appropriate iso-Doppler contour for pixel ij.

are $\mathbf{R}_{\mathrm{T}} = (x_{\mathrm{T}}, y_{\mathrm{T}}, z_{\mathrm{T}})^T$, where x_{T}, y_{T} and z_{T} satisfy a relationship which constrains the point to the surface of an earth model such as

$$\frac{x_{\mathrm{T}}^2 + y_{\mathrm{T}}^2}{(R_E + h)^2} + \frac{z_{\mathrm{T}}^2}{R_P^2} = 1, \tag{24}$$

an ellipsoid of revolution with local topographic elevation $h = h(x_{\mathrm{T}}, y_{\mathrm{T}}, z_{\mathrm{T}})$ and $R_P = (1 - f)(R_E + h)$. The geoid, or base ellipsoid with $h \equiv 0$, has semi-major (equatorial) axis $R_E = 6378.138$ km and the *flattening* factor $f = 1/298.255$. In discussing terrain correction we shall see that, even for moderately varying terrains with smooth topographic functions h, the intersection of the side looking radar beam centroid and the earth may not be unique or even well defined. For this reason it is best to assume a constant mean image elevation h during the geolocation algorithm, then subsequently correct for local terrain variations. Also, as for tiepointing, the topographic function, or digital elevation model (DEM) in discrete form, is only available for planetary surfaces which have been previously mapped in detail.

The coordinates of a target are also rotating with the earth so that its velocity vector in the GEI system is

$$\mathbf{V}_{\mathrm{T}} = \overrightarrow{\omega_e} \times \mathbf{R}_{\mathrm{T}}, \tag{25}$$

where we use vector product notation. The position of $\mathbf{R}_{\mathrm{S}} = (x_{\mathrm{S}}, y_{\mathrm{S}}, z_{\mathrm{S}})^T$ and velocity $\mathbf{V}_{\mathrm{S}}$ of the spacecraft are known as functions of time from tracking data and are provided as ephemeris information in the image header data records. Thus for a target pixel at azimuth line i and range sample (or *bin*) j, the target to sensor position vector is

$$\mathbf{R}_{ij} = \mathbf{R}_{\mathrm{S}}(t_{ij}) - \mathbf{R}_{\mathrm{T}}, \tag{26}$$

where t_{ij} is the time at which the beam centroid intersects the target location. The slant range R is then a function of $(x_{\mathrm{T}}, y_{\mathrm{T}}, z_{\mathrm{T}})$,

$$R = R(x_{\mathrm{T}}, y_{\mathrm{T}}, z_{\mathrm{T}}) = |\mathbf{R}_{ij}|. \tag{27}$$

For our given target pixel, the range R_{ij} is known from pulse travel time. This forces the location $(x_{\mathrm{T}}, y_{\mathrm{T}}, z_{\mathrm{T}})^T$ to lie on the nearly circular intersection of the sphere of radius R_{ij} around the sensor position,

$$|\mathbf{R}_{ij}|^2 = R_{ij}^2, \tag{28}$$

and the earth surface model (24).

A final constraint (three equations in the three unknowns x_{T}, y_{T} and z_{T}) is needed to fix the pixel location uniquely. This is provided by the Doppler equation. Recall Equation (12) from Section 2.2.1 giving the Doppler shift as the beam passes the target,

$$f_D = -\frac{2}{\lambda}\frac{dR}{dt}. \tag{12}$$

Let $\mathbf{R}_{ij} =: (x, y, z)^T$ so that $x := x_{\mathrm{S}} - x_{\mathrm{T}}$, $y := y_{\mathrm{S}} - y_{\mathrm{T}}$ and $z := z_{\mathrm{S}} - z_{\mathrm{T}}$. Then

$$R = \sqrt{x^2 + y^2 + z^2} \tag{29}$$

and, using the dot notation for time differentiation,

$$\dot{R} := \frac{dR}{dt} = \frac{x\dot{x} + y\dot{y} + z\dot{z}}{\sqrt{x^2 + y^2 + z^2}}. \tag{30}$$

Since $(x, y, z)^T = \mathbf{R}_{\mathrm{S}} - \mathbf{R}_{\mathrm{T}}$ and $(\dot{x}, \dot{y}, \dot{z})^T = \mathbf{V}_{\mathrm{S}} - \mathbf{V}_{\mathrm{T}}$, we have from (12), (29) and (30)

$$f_D = -\frac{2}{\lambda R}(\mathbf{R}_{\mathrm{S}} - \mathbf{R}_{\mathrm{T}}) \cdot (\mathbf{V}_{\mathrm{S}} - \mathbf{V}_{\mathrm{T}}) \tag{31}$$

where the dot here denotes the scalar product of vectors. This relates f_D to quantities which are known, λ, $\mathbf{V}_{\mathrm{S}}$, $\mathbf{R}_{\mathrm{S}}$, and to quantities which depend on $(x_{\mathrm{T}}, y_{\mathrm{T}}, z_{\mathrm{T}})$, namely R and $\mathbf{R}_{\mathrm{T}}$ since $\mathbf{V}_{\mathrm{T}}$ depends on $\mathbf{R}_{\mathrm{T}}$ by (25).

Now, given a range R_{ij} and a Doppler centroid f_D which have been computed for this pixel by the SAR processor, the three equations (24), (28) and (31) can be solved numerically for the earth location coordinates $(x_{\mathrm{T}}, y_{\mathrm{T}}, z_{\mathrm{T}})^T$.

4.1.2 *Geocoding Algorithms*

The ultimate objective of geolocation is *geocoding*, the presentation of the data on a map grid such as Universal Transverse Mercator or Polar Stereographic. It is possible to apply the location equations to every pixel to solve for the GEI coordinates, convert to geographic coordinates and thence to map grid coordinates. Symbolically

$$(i, j) \longleftrightarrow (R, f_D) \longleftrightarrow (x, y, z) \tag{32}$$

$$(x, y, z) \longleftrightarrow (R_e, \mathrm{lat}, \mathrm{long}) \tag{33}$$

$$(\mathrm{lat}, \mathrm{long}) \longleftrightarrow (X, Y) \longleftrightarrow (p, q) \tag{34}$$

Where i and j are slant range image pixel numbers, R and f_D are slant range and Doppler centroid, x, y and z are GEI coordinates, R_e, lat and long are local earth radius and geographic coordinates, X and Y are easting and northing in meters, and p and q are geocoded map grid image pixel numbers.

Solving the location and conversion equations, however, is computationally expensive. Only minor distortion is introduced if, instead, the geocoding procedure is approximated locally by two simpler two-dimensional transformations consisting of a *geometric rectification* and a *geometric rotation*. By choosing the intermediate coordinate system for the rectified image to correspond to natural geometric relationships between sensor and earth surface, it is possible to make the intermediate transformation bilinear in the coordinates and so easily controlled analytically and computationally. Then the final transformation takes the form of rotation of the natural coordinates to map grid north, again a simple procedure. Thus let r be the ground range distance in the across track direction and s be the distance along the nadir track. Then each pair (r, s) corresponds to an earth location and we seek transformations to perform

$$(R, f_D) \longleftrightarrow (r, s) \tag{35}$$

$$(r, s) \longleftrightarrow (X, Y). \tag{36}$$

Transformation (36) is the rotation to map north and can be computed from the angle β of the nadir track with respect to north. To get β use geolocation ((32)–(34)) on two iso-range points (i_1, j) and (i_2, j), difference their (X, Y) coordinates and set $\beta = \arctan(\Delta Y / \Delta X)$.

Now it is possible to use (32), (33), (34), (36) to map $(i, j) \leftrightarrow (r, s)$. Do this for the corner pixels of the input slant range image to get the corners in the rs-plane. Then subdivide this image rectangle into uniform rectangular sub-blocks of convenient size (about 50 pixels square). Use (36), (34), (33), (32) to correspond these corners to the input image. Now we have enough information to construct the rectification approximation (35) as a bilinear interpolation between the rs rectangular sub-blocks

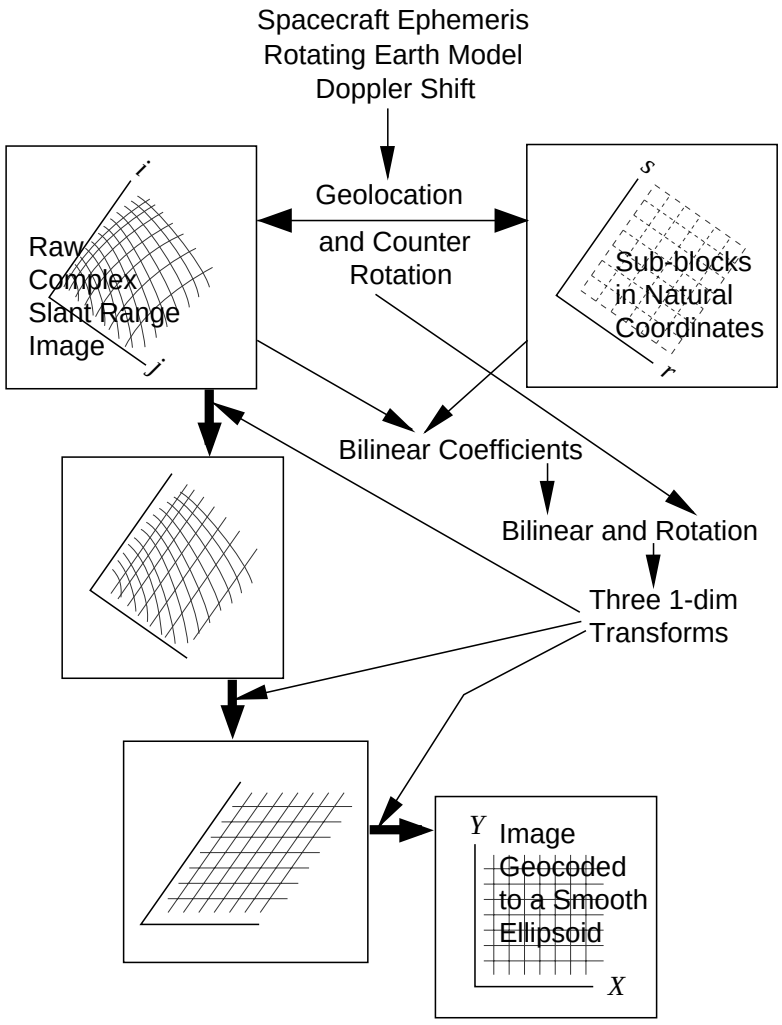

Figure 6. Block diagram of the geocoding procedure. The thin arrows indicate derivation and application of parameters. The thick arrows denote resampling transformations of the image data.

and the corresponding quadrilaterals in the ij-plane of the input image. Repeat this procedure for each sub-block to process the entire image.

The composed transformation (35), (36) is most efficiently implemented by combining the bilinear interpolation and the rotation analytically, and then factoring the resulting transformation into three one-dimensional resampling passes, involving bilinear rectification in azimuth, range rectification and vertical shear, and horizontal shear. The two shear transformations combine to produce a rotation. This procedure is represented schematically in Figure 6. See Curlander and McDonough [1991, Ch. 8.3.3] for details.

As indicated by the arrows in (32)–(36) the transformation can go both ways. Thus a slant range image pixel (i, j) may be mapped into a geographic location. Conversely, given a point on the earth, the line and sample numbers and incremental distance to the

nearest image pixel can be found. In either case the output image must be resampled. The numerical procedures are different, of course, but the computational complexity is equivalent for either direction. These considerations are important when the geocoded output image is tied to another raster product such as a DEM for terrain correction, or an image from another remote sensing instrument. This will be discussed in greater detail in the sections on terrain correction and multisensor registration.

4.2 *TERRAIN INDUCED DISTORTION*

For an imaging radar it is the side or slant looking geometry which permits range discrimination. At the nadir there is a discontinuity in change in ground range r with change in slant range R. Referring to Equation (D7) in Appendix D, we see that $dr/dR = R_e/(R_e + H)\sin\theta$, where θ is *look angle*, so that the ground range resolution is infinite at $\theta = 0$. This is apparent from the flat earth approximation of Figure 7a, where, by simple trigonometry, $\Delta r = \Delta R/\sin\theta$. Thus the look angle must be large enough so that reasonable range resolution is achieved, but not so large that incidence is grazing and backscatter is lost. Other considerations, such as swath width, range return ambiguities, and the strong dependence of scattering on incidence angle, influence the choice of look angle for a particular SAR instrument and environment. The practical range is about 20° to 50° with some instruments, such as Radarsat, capable of varying the look angle.

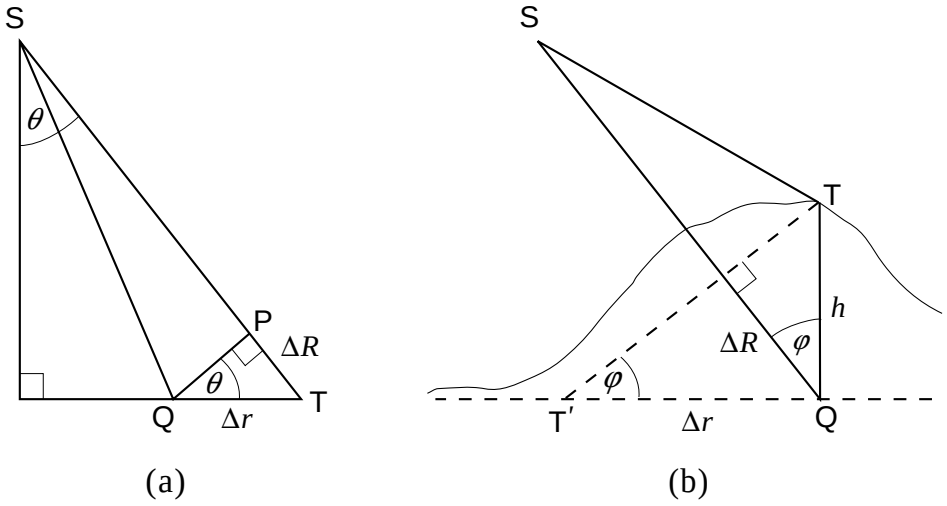

Figure 7. Sensor S is looking down at target T at look angle θ which, for a flat earth, is the same as incidence angle φ. In (a) on the left we make the approximation that R is much greater than ΔR so that isosceles triangle SPQ has a very short base and $\angle$SPQ is very nearly right. In fact $\Delta R/R \approx 10^{-5}$. In (b) the target is elevated to a height h which results in a slant range shortening of ΔR and a ground range displacement of Δr. Here the approximation is that isosceles triangle STT′ has a relatively short base TT′ compared to the slant range, so that SQ is approximately perpendicular to that base. This is justified by $h \ll R$. The worst case in the ASF station mask and, in fact, on planet Earth, is Mt. McKinley for which $h/R \approx 6 \times 10^{-3}$.

Whatever angle optimizes the tradeoffs mentioned above, the mere fact of ranging and side looking will produce some geometric distortion when imaging anything other than a simple smooth surface. Figure 7b illustrates the basic phenomenon whereby a target which is elevated by local relief to a height h above the geoid will be displaced in ground range by an amount $\Delta r = h/\tan\varphi$.

4.2.1 *Foreshortening, Layover and Shadowing*

Such a height dependent range correction can be applied to an elevated area in an image which covers many pixels and has average elevation h and relatively low variation. For terrain where the scale of the relief is comparable to the SAR resolution, the situation is more complicated. Scattering occurs from sloping and faceted surfaces which creates local distortion that depends on the surface to beam orientation and which may not be recoverable, i.e., information is lost.

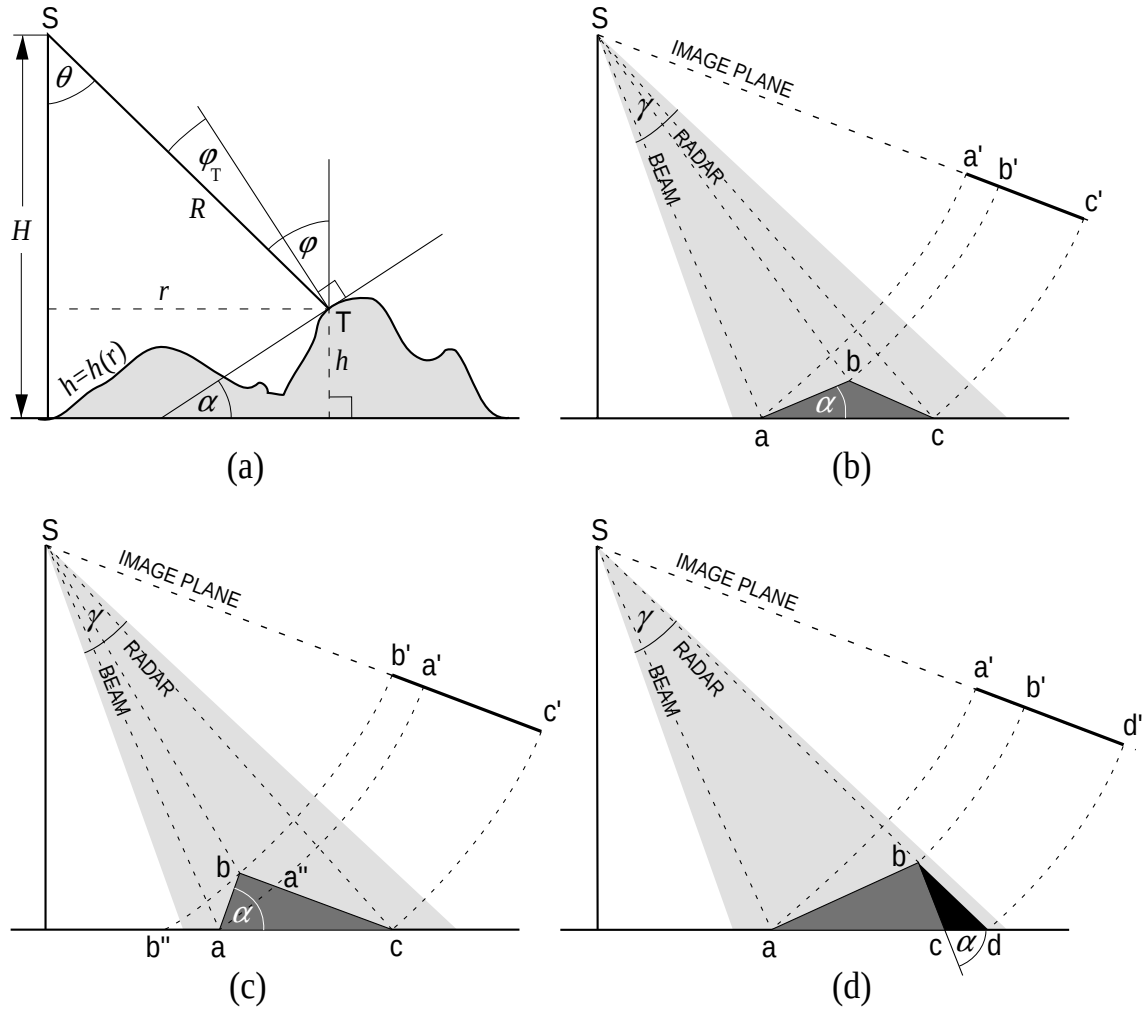

Figure 8. (a) Terrain imaging geometry of side looking radar. The remaining panels schematically illustrate forms of distortion induced by projecting terrain a b c along equal slant range arcs into a′b′c′ in the image plane. These are: (b) foreshortening, (c) layover, (d) shadowing.

Referring to Figure 8, we make a flat earth approximation which does not alter the geometric relationships and greatly simplifies the computations. More exact formulas for a spherical earth are given in Appendix D. In panel (a) we show the basic geometry of the cross section including the sensor S, target T and nadir point. This plane intersects the surface in an iso-azimuth line. Sensor height is H, slant range is R and ground range is r. Along this section the surface relief is given as a function $h(r)$ of ground range. For simplicity we assume that h is continuous and single valued which excludes vertical or overhanging terrain. Let the tangent to h at T make angle α with the r-axis so that $\tan\alpha = dh/dr$. This is the *terrain slope*. For a flat earth the (global) *incidence angle* φ, defined as the angle from the local vertical to the slant range vector, is the same as the look angle θ between nadir vertical and the range vector. As a sensor parameter the look angle is a constant fixed by antenna orientation and spacecraft attitude. For this analysis we let θ vary throughout the vertical beamwidth γ of the radar. The *local incidence angle* $\varphi_{\rm T}$ is measured from the normal to the surface relief (perpendicular to its slope) to the slant range vector. Simple geometry shows that $\varphi_{\rm T} = \varphi - \alpha$ and

$$\begin{aligned} \sin\theta &= r/R \\ \cos\theta &= (H-h)/R. \end{aligned} \tag{37}$$

Figure 8b illustrates *foreshortening*. The simplified terrain element (hill) a b c is illuminated by the shaded radar beam and the echoes from points a, b and c are received at travel times that correspond, in the slant range image plane, to a′, b′ and c′. It is clear that when $\overline{\rm ab}$ is sloped toward S, but only so much that $\alpha < \varphi$, then the image $\overline{\rm a'b'}$ will be shorter than $\overline{\rm ab}$. When the slope is perpendicular to the beam, i.e., $\alpha = \varphi$, a′ will coincide with b′ so that all the energy scattered from the slope will be compressed into a single pixel. This is complete foreshortening and marks the transition to *layover* shown in panel (c).

Here $\alpha > \varphi$ and consequently b′ precedes a′ in range sequence. The echo from $\overline{\rm ab}$ is distributed, but in reverse sequence and superimposed over that from $\overline{\rm ba''}$. The steep foreslope $\overline{\rm ab}$ is called the *active* layover region and the backslope $\overline{\rm ba''}$ is the far range *passive* layover region. It would not be distorted on its own right, but is involved in layover because of its proximity to the steeper slope. Similarly there is a near range passive layover region from b″ to a. Energy scattered from there is also superimposed onto $\overline{\rm b'a'}$ in the image plane. Thus, without making assumptions about the nature of the scattering material, we cannot distinguish the echoes from the three regions. At best we can split them up, weighted according to their sizes and slopes, and redistribute the intensities along the surface b″ a b a″. Fine tuning of the radiometric correction can be applied by adjusting for the factors in the radar Equation (22) which are sensitive to the relative position of sensor and target.

A third configuration is illustrated in Figure 8d where the back slope $\overline{\rm bc}$ of the terrain is steep enough so that it cannot be illuminated by the radar beam. This occurs when the slope is negative and $\alpha \le \theta - 90°$, and is known as *shadowing*. Backscatter information is lost, not only from area $\overline{\rm bc}$ (which, strictly speaking, is obscured rather than shadowed), but also from $\overline{\rm cd}$ which is shadowed in the proper optical sense of the

word. As in layover, these are referred to as *active* ($\overline{\text{bc}}$) and *passive* shadow regions. In general active regions can be distinguished by their slope, while passive regions are determined by their proximity to active ones. Regardless of such distinctions, no information is returned from the entire region $\overline{\text{bcd}}$. Consequently only noise appears in region $\overline{\text{b}'\text{d}'}$ in the image plane.

The schematics of Figure 8 are simplifications. Continuously sloping and rapidly varying terrains in real earth applications have the possibility of overlapping between layover regions as well as shadowing layover regions. Not all logical combinations are physically possible, so any algorithm for locating and compensating for these effects must make a careful case-by-case analysis. Such an algorithm [Kropatsch and Stroble, 1990] scans iso-azimuth lines and computes the local slope from the topographic function $h(r)$, and the incidence angle from h and R, using (37) for a flat earth. Local incidence angle φ_{T} is their difference and active layover occurs when $\varphi_{\text{T}} < 0$. Active shadowing occurs when $\varphi_{\text{T}} \geq 90°$. These conditions can be related to easily computed quantities by differentiating $R^2 = r^2 + (H - h(r))^2$ with respect to r to obtain

$$R\frac{dR}{dr} = r - (H - h)\frac{dh}{dr} = R(\sin\theta - \cos\theta\tan\alpha). \tag{38}$$

The trigonometric expression comes from (37) and implies that the (flat earth) layover condition, $\alpha > \theta$ is equivalent to the geometrically intuitive condition $dR/dr < 0$. Since always $R > 0$, (38) implies layover when

$$\Lambda(r) := r - (H - h(r))\frac{dh}{dr} < 0. \tag{39}$$

Similarly, differentiating $\tan\theta = r/(H - h(r))$, and applying (37) gives

$$R^2\frac{d\theta}{dr} = H - h + r\frac{dh}{dr} = R(\cos\theta + \sin\theta\tan\alpha). \tag{40}$$

Then the (flat earth) shadowing condition $\alpha \leq \theta - 90°$ becomes $d\theta/dr \leq 0$, i.e., incidence angle decreasing with ground range. Again, since $R^2 > 0$ this is computationally the same as

$$\Sigma(r) := H - h(r) + r\frac{dh}{dr} \leq 0. \tag{41}$$

4.2.2 *Terrain correction*

In Section 4.1.1 the geolocation equations are described for a smooth ellipsoid with an average elevation. After this kind of geocoding, subsequent processing can be performed in which the image is corrected for local relief given by a DEM. The idea is to remove the displacement Δr due to the side looking geometry as illustrated in Figure 7a. Thus we translate the intensity of the slant range image by an amount appropriate for the terrain elevation.

The first step, using geocoding, is to compute the slant range image pixel coordinates (i', j') corresponding to the map grid pixel numbers (p, q) at which the elevation is known. We use primes on i and j to indicate that they are not necessarily integers, or even within the original SAR image, but are merely the values in the line-pixel coordinate system of that image determined from the geocoding transformations. If the location is off the original image, the map grid pixel will be null (no data). Otherwise, the displacement can be computed from ΔR as in Figure 9. In this second step $\mathbf{R}_{\mathrm{T}}(0)$ is computed from the geographic coordinates (ζ, χ) corresponding to (p, q). Earth corotating cartesian coordinates are used to express the location vectors $\mathbf{R}$. The transformation depends on the geoid model (24), and is given in Curlander and McDonough [1991, p. 404]. This transformation also permits calculation of $\mathbf{R}_{\mathrm{T}}(h)$ as $\mathbf{R}_{\mathrm{T}}(0)+h\mathbf{u}$, where $\mathbf{u}$ is the unit normal vector to the geoid at Q, $\mathbf{u} := (\cos\zeta\cos\chi, \cos\zeta\sin\chi, \sin\zeta)^T$.

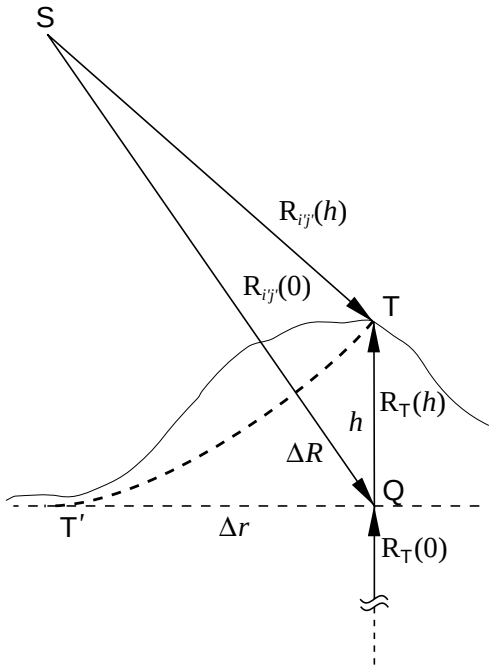

Figure 9. A more precise schematic of the geometry of relief displacement for side looking radar. Compare with Figure 7b. The position vectors are shown for a target on terrain elevated a distance h above the surface of the geoid, $\mathbf{R}_{\mathrm{T}}(h)$, and for the target as geolocated on the base ellipsoid, $\mathbf{R}_{\mathrm{T}}(0)$.

The third step calculates the spacecraft position $\mathbf{R}_{\mathrm{S}}$ as a function of time which is directly related to the azimuth location i'. We can then form the range vectors $\mathbf{R}_{i'j'}(0)$ and $\mathbf{R}_{i'j'}(h)$ from formula (26) and finally the displacement in slant range as

$$\Delta R = |\mathbf{R}_{i'j'}(h)| - |\mathbf{R}_{i'j'}(0)|. \tag{42}$$

The displacement in pixel coordinates is

$$\Delta j = 2f_s\Delta R/c, \tag{43}$$

where f_s is the range sampling rate and c is the wave propagation speed which is approximately the speed of light. An azimuth displacement Δi can be calculated by substituting the two range vectors at height 0 and h for $\mathbf{R}_{\mathrm{S}} - \mathbf{R}_{\mathrm{T}}$ in (31). This gives f_D as a function of height so that differencing the two values provides $\Delta f_D = f_D(h) - f_D(0)$ and the azimuth displacement is

$$\Delta i = \Delta f_D \times \mathrm{PRF}/f_R(h), \tag{44}$$

where the pulse repetition frequency (PRF) is the azimuth sampling rate and the Doppler rate f_R is calculated from (21) at the range corresponding to the elevated target.

We now know that the scattering intensity corresponding to the elevated target at map location (ζ, χ) and grid pixels (p, q) occurs at slant range image pixel coordinates $(i' + \Delta i, j' + \Delta j)$. Values from the nearest integer pixel numbers are interpolated to these coordinates and the resulting DN is placed at map grid pixel number (p, q).

4.2.3 *Two Stage Terrain Corrected Geocoding, SAR Image Synthesis*

The complete SAR image processor will combine the methods of Sections 4.1.2, 4.2.1 and 4.2.2 to produce an output image which has been geometrically, geographically and radiometrically corrected. Since terrain correction requires that the image be registered to the geographically more precise DEM, it is necessary to make a fine location adjustment after the geocoding procedure. This can be done by an automated tiepointing procedure based on synthesizing the SAR image from the DEM. Thus a simplified backscattering model is derived from the SAR scanning configuration, the radar characteristics, and the surface relief as specified by the DEM data. The result is a synthetic image which shows the major features of the geocoded SAR data, but is located by the geographic coordinates of the DEM. Comparing (patches of) these two images by means of two-dimensional area cross-correlation will determine whatever small shift is required to bring them into registration. This correction is then applied to the geocoded image.

Figure 10 shows a complete post-geocoding geometric/radiometric correction procedure for eliminating terrain induced distortion. The output products include the incidence angle map which gives the local incidence angle at each pixel. This auxiliary image can be combined with the completely corrected image and scattering *vs.* incidence angle curves to produce a uniform image of the surface brightness. The shadow and layover masks can be layered into the final image in order to assess the information content on a pixel by pixel basis.

This two stage geocoding, where the terrain correction is done in a second pass, has become the standard method for NASA/JPL installations [Kwok *et al.*, 1987]. The separation into two passes is necessary since the geolocation equations (32) are not always uniquely solvable if the earth model includes terrain. Complete foreshortening and layover (§4.2.1) will induce a many to one nature in the relationship $(x, y, z) \longrightarrow (i, j)$, i.e., many surface points may be mapped onto one pixel. Therefore, if we try to solve the location equations directly using $\mathbf{R}_{\mathrm{T}}(h(r))$ to compute the slant range, we may not get the correct geographic position.

4.2.4 *Inverse Geolocation and Single Stage Geocoding*

If, however, we invert the problem and solve for pixel location from geographic location, the mapping is unique. Aside from highly reflecting small targets which create supersaturated pixels, each resolution element is, by design, mapped onto only one image pixel. Thus we can incorporate elevation data into the earth model, using $\mathbf{R}_{\mathrm{T}}(h) = \mathbf{R}_{\mathrm{T}}(0) + h\mathbf{u}$, and so do geolocation and terrain correction in one step. There

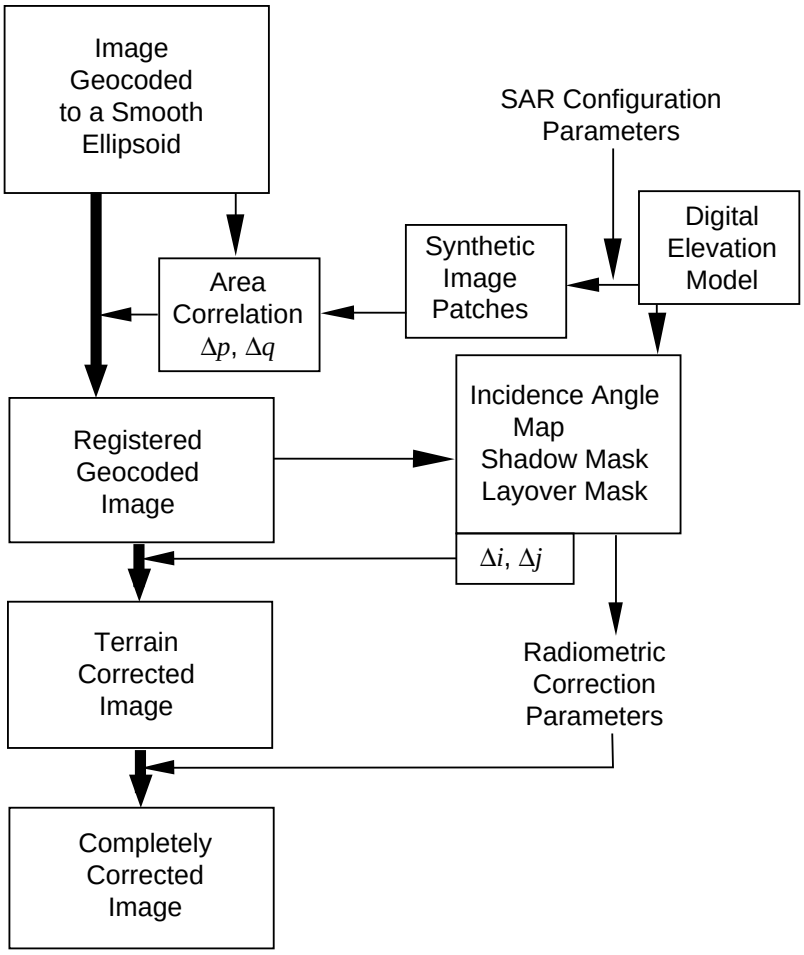

Figure 10. Block diagram of the terrain correction procedure. The thin arrows indicate derivation and application of parameters. The thick arrows denote resampling transformations of the image data.

are, however, some new requirements. For instance, we must extend the discrete image data for range R and Doppler shift f_D to continuous functions of the image space coordinates (i', j'). This extension is done by standard interpolation/extrapolation techniques, after which the analytical approximants to R and f_D can be differentiated so that Newton's method can be used to solve for an (i', j') corresponding to a geographic location. Then the brightness value of the pixel closest to (i', j') can be placed in the geographically and topographically correct position. This method has been implemented by investigators at the German Aerospace Research Establishment (DLR) [Roth *et al.*, 1989; Schreier *et al.*, 1990]. It has the additional advantage that the relatively more precise DEM positions can be used as the starting point and the image resampled to match.

A variation on the inverse method has been developed by the Science and Applications branch of the USGS EROS Data Center (EDC) [Wivell *et al.*, 1992]. They simplify the solution procedure by reducing the root search to one dimension, namely time t. Thus, given a (lat, long, elev) location on the earth surface, its GEI coordinates

$\mathbf{R}_{\mathrm{T}}(t)$, depend on time according to sidereal rotation. Similarly, from orbit ephemera, we know $\mathbf{R}_{\mathrm{S}}(t)$ and so slant range $|\mathbf{R}_{\mathrm{S}} - \mathbf{R}_{\mathrm{T}}|$. In fact both $\mathbf{R}_{\mathrm{T}}$ and $\mathbf{R}_{\mathrm{S}}$ can be modelled accurately as harmonics in time with coefficients fitted to empirical data. Range and azmuth sampling rates for a given image then convert $(t, R(t))$ directly to pixel coordinates (i', j'). Thus for a DEM location in an image we have $t \mapsto (i', j')$. To complete the SAR model we must also satisfy the Doppler data $f_D(i, j)$ which is given with the image. Differentiation, ephemeris and differencing variously give us $\mathbf{V}_{\mathrm{S}} - \mathbf{V}_{\mathrm{T}}$ and $\mathbf{A}_{\mathrm{S}} - \mathbf{A}_{\mathrm{T}}$, so that we can compute $f_D(t)$ from (31) and df_D/dt by differentiating (31)

$$\frac{df_D}{dt} = -\frac{2}{\lambda R}\Big((\mathbf{R}_{\mathrm{S}}-\mathbf{R}_{\mathrm{T}})\cdot(\mathbf{A}_{\mathrm{S}}-\mathbf{A}_{\mathrm{T}})+|\mathbf{V}_{\mathrm{S}}-\mathbf{V}_{\mathrm{T}}|^2-((\mathbf{R}_{\mathrm{S}}-\mathbf{R}_{\mathrm{T}})\cdot(\mathbf{V}_{\mathrm{S}}-\mathbf{V}_{\mathrm{T}})/R)^2\Big). \quad (45)$$

Using our time to pixel mapping we then solve

$$\Delta f_D := f_D(i'(t), j'(t)) - f_D(t) = 0 \quad (46)$$

for t using the Newton time update

$$\delta t = \Delta f_D \Big/ \frac{df_D}{dt}. \quad (47)$$

Iteration finally provides the desired correspondence of geography to image. SAR image synthesis is also used in this method for fine tuning the registration of the raw image to the DEM.

A prototype of the EDC geocoding method has been coded in C for a Sun 4/60 Unix system. At present (late 1992) it is in beta test at ASF. EDC plans to integrate the code as a module in their Land Analysis System (LAS), a general purpose image processing system designed for land applications.

4.3 *IMAGE TO IMAGE REGISTRATION*

Individual SAR images are a rich source of information on their own. Combined with other SAR images to get wider area coverage, or with other remote sensing data to compare with emissions in different spectral bands, the depth of interpretation is multiplied manyfold. The primary problem in merging these disparate sources is geographic co-registration of the imagery. Geocoding accuracy is generally less precise than the pixel size, especially the 10 to 12.5 meter pixels of Landsat/SPOT and ERS-1, respectively. Techniques depending on the data itself, such as the correlation between raw and synthesized SAR images discussed in §4.2.3, are necessary to achieve the requisite accuracy.

The prototypical data dependent co-registration method is tiepointing, as discussed in §4.1. Aside from the objections raised there, a serious drawback to the method is the need for operator interaction in choosing the tiepoints. Area cross-correlation, in a sense, automates the tiepoint selection, but has problems when there are significant differences between the two images of the same surface. These may be

due to temporal or geometric differences between SAR passes, or to sensor differences between SAR and other imaging instruments. To solve this problem we will consider, in a later section, pattern recognition methods for correlating images.

4.3.1 *Mosaicking*

As noted, SAR, like any remotely sensed image, comes in discrete chunks. For a synoptic picture the pieces must be assembled into a coherent whole. Hence, the jaw cracking participle 'mosaicking', a word most lexicographers would refuse to consider. For image processors, however, it is a realistic verb.

The geocoding procedures put all of the component images into a common, co-registered map grid database. It is possible to mosaic SAR images which have been geolocated and gridded, but not terrain corrected. Since, however, the geometric displacement caused by terrain relief depends on global incidence angle which varies across the image with range, matching up adjacent orbit swaths would encounter a mismatch due to unequal distortion at near and far range. For situations where the resolution is coarse and the relief is moderate compared to the altitude of the SAR, such as Magellan images of Venus, terrain correction is not necessary. For full resolution ERS-1 or Seasat, however, there will be visible distortion at the seams in areas with significant relief. Thus terrain correction is a desirable pre-mosaicking step.

Even with the refined accuracy achieved through DEM synthesis area correlation, image features may not be precisely registered between frames of a mosaic. Two-dimensional cross-correlation of patches within the overlap area will provide the number of pixel offsets required to bring the image frames into best possible alignment.

Further problems arise from uneven radiometric intensity due also to range variation in incidence angle. Examples shown in Kwok *et al.* [1990b] of Seasat mosaics have distinctly perceptible seams at the swath boundaries. More exacting radiometric calibration in ERS-1 SAR processing eliminates much of this variation, and scenes mosaicked by direct concatenation show seams due principally to variation in backscatter from actual surface phenomena. This impediment to mosaicking can be dealt with by choosing scenes which have been taken under closely matching conditions. Otherwise considerable effort must be undertaken to classify and combine image characteristics. Such considerations are more important with optical and other multispectral sensors which are sensitive to clouds, snow, vegetation color, dust and other ephemeral phenomena.

SAR has only one band, but is sensitive to changes in soil and vegetation moisture, multiple scattering, ice, and particularly surface roughness on bodies of water which may cause wide variation in backscatter from such surfaces. Kwok *et al.* [1990b] describe a *feathering* technique for blending across such discontinuities at image boundaries. They select a strip along the seam which is wider than the overlap area. A mean value is determined from the overlap area and is used to interpolate the image intensities linearly across the transition strip. This creates a trade-off, depending on the width of the feathering strip, between calibration accuracy and the consistency of the mosaic.

4.3.2 *Composite SAR Imagery*

In §4.2.1 we discussed how foreshortening, layover and shadowing can introduce, not only geometric distortion, but also radiometric errors due to excess energy in the foreshortened and laid over areas and too little scattering from the shadowed zones. There are sophisticated procedures for correcting these effects which use geometric and empirical modelling of radar backscatter, but which also involve considerable ancillary data from the imaged surface [Bayer *et al.*, 1991].

Furthermore, it is not always, desirable to remove terrain influences entirely, as the "shaded relief" effect gives valuable information about the surface. What is desired is a correction of the apparent inhomogeneities in backscatter intensity. Thus for a simple expedient, we note that, with moderate relief, the backslopes of terrain features are distorted much less than the foreslopes (Figure 8b). For backslopes incidence is more grazing but backscatter from most land surfaces is comparable to that for standard look angle incidence. Thus by combining SAR images of the same surface but from opposite look directions, we can get backscatter information from backslopes in all cases and so eliminate the radiometric error due to foreshortening. This can be done with passes from ascending and descending orbits of the ERS-1 SAR satellite which have a look direction separated by about 140°.

For steeper relief the foreslopes will be brightened and the backslopes may be shadowed. Then both aspects are in error and a composite image can only replace lack of information with distorted information. But if backslopes are illuminated, choosing the less bright pixel between ascending and descending passes will provide a substantial increase in information. In fact, a minimum acceptance procedure will eliminate any anomalous brightening, not only that due to terrain. Thus speckle (§3.4.2), which commonly produces extreme pixel values, is spatially random. Therefore it is unlikely to occur in the same place in both images and so will be eliminated. Similarly, bright returns from wind roughened water will survive in the composite image only if the wind is comparable at the time of both passes. Thus we see that, in a general sense, anomalous pixel values due to anisotropy or ephemeral events will tend to be moderated by this procedure.

Similarly, if the maximum is chosen, anomalously dark pixels (shadowing, dark speckle) will be eliminated in favor of pixels more likely to represent true backscatter values. To combine the virtues of each of these selection criteria, choose the pixel which has value closest to a statistically typical value such as the mode or median of the image DN distribution. Then both high and low extremes will be moderated in favor of more likely values. Such a procedure has been implemented by EDC [Wivell *et al.*, 1993] and applied with good results to an area in the interior of Alaska near Tanana.

4.3.3 *Multisensor Image Registration*

The problem in creating a layered product from multiple sensors (say SAR and Landsat) is in assuring pixel to pixel registration, else the resulting image is muddied and interpretation is difficult. For this process to be automatic, the comparison of the two images must depend only on their content and not require operator selection of

features. Thus the essential problem is automatic feature or pattern recognition and comparison.

There is a large variation in response of different sensors to the same surface. SAR can be bright when Landsat is dim and vice versa. Topography is prominent in SAR but not Landsat. Landsat sees roads and rivers well but SAR does not. Thus feature extraction must be very general to compare well between sensors. Investigation [Rignot *et al.*, 1991] has shown that some classification schemes can segment images from different sensors into comparable regions. Similarly, edge detection algorithms of a kind which are insensitive to the multiplicative speckle noise in SAR, will produce linear features that compare well between images. Details are given in Rignot *et al.* [1991].

Following selection of common features, their locations must be geometrically matched in order to determine the optimal registration correction. This can be done in a number of ways. The features can be represented as binary images and area correlation applied to find the misregistration shifts. Other methods, known as distance transform and chamfer matching, use a generalized distance to quantify the mismatch between features. Optimizing this distance as a function of shift determines the correction. These methods work well if the features are close in shape and orientation. For more severely mismatched features dynamic programming/autoregressive model methods may be tried.

However the matches are found between patches of the different images, some kind of constraint filtering must be done on the matching events to eliminate erroneous matches. Such methods and test results are discussed in Rignot *et al.* [1991] and Curlander and McDonough [1991, Ch. 8.4.2].

Automated multisensor image registration is still a very experimental field. Techniques are at present *ad hoc* and selectively applied as required by the data under consideration. Full automation will probably require an artificial intelligence/expert system approach with considerable compute power available for trial and error or brute force methods.

Chapter 5
Geophysical Applications Processing

Because of the sensitivity of SAR to surface roughness with dimensions on the order of the wavelength of the radar signal (5.7 cm for ERS-1, 23.5 cm for JERS-1), applications in physical oceanography such as polar sea ice and wind/wave/current sea surface phenomena are particularly apt. Accordingly NASA/JPL has developed a Geophysical Processor (computer) System (GPS) at ASF which performs secondary analysis (level 2 and 3 derived data products) on the raw imagery (level 1 products, see Appendix C) to produce information concerning some physical properties of the ocean surface. The user interface for this system is described in Baltzer *et al.* [1991].

There are currently three functions performed by the GPS: (a) Tracking of the motion of sea ice from pairs of images separated in time; (b) Ice type classification; and (c) Wave spectra analysis.

5.1 *ICE MOTION TRACKING*

Collaboration between SAR image processing specialists and sea ice geophysicists has resulted in a uniquely specialized computer system which tracks the drift of the ice by matching common ice floes and lead patterns in SAR image pairs which are separated by time intervals, most commonly multiples of 3 days (the orbit repeat period for the ice phase of the ERS-1 and other SAR missions), [Kwok *et al.*, 1990a].

Candidate pairs are selected from the image database by an algorithm which uses wind and drift buoy data from ancillary data sets to predict the most likely ice velocity. A similar but more synoptic analysis is presented by Dade *et al.* [1991]. There mean ice motion is coordinated with ERS-1 swath coverage to estimate statistically the expected image pair overlap (or repeat coverage) of sea ice throughout the Arctic. This guide is designed to assist the sea ice motion investigator in making informed selection of ERS-1 images for input to the GPS.

The pattern matching algorithm used to find the displaced location of sea ice features is a combination of techniques such as hierarchical area correlation and boundary shape correlation (the so-called (ψ, s) method). These techniques are applied selectively depending on the amount of deformation and/or rotation between the imaged ice patches. Rigid translation is easy to recognize. Motion which alters the shape or orientation of the features requires more sophisticated analysis. Various kinds of constraint filtering and consistency checks are applied to exclude mismatched patterns and an overall quality assessment is provided. Image pairs which lead to low quality estimates are referred to the system operator for visual evaluation. Details and further references are in Kwok *et al.* [1990a].

The output of the GPS ice tracker is a 100×100 km grid with 5 km spacing on a Polar Stereographic map projection. This has been chosen to match the data format of the Scanning Multichannel Microwave Radiometer (SMMR), another spaceborne instrument (passive microwave) useful for understanding sea ice. At each grid point where motion information has been found, a displacement vector is presented. These can be plotted to show a vector field which gives the approximate streamlines of the bulk flow of the ice in a fixed (Eulerian) coordinate system.

5.2 *ICE TYPE CLASSIFICATION*

A very important question for polar ocean and atmospheric research concerns the distribution of ice thickness, ice age and its variation throughout the year. Field observations have shown that, under most winter conditions, sea ice can be classified with 95% confidence into four age categories: (a) Multi-year ice; (b) First-year ice; (c) New ice; and (d) Open water.

This scheme is based on an empirical relationship between ice type and its backscatter brightness at a given temperature. The algorithm begins by segmenting the image into as many as eight classes using clustering. Then temperature is determined from ancillary meteorological or remote sensing data and the appropriate table of brightness *vs.* age consulted in order to make a maximum likelihood assignment of ice types to the classes [Holt *et al.*, 1990a].

There are two major difficulties with this method. The first is due to the widely variable brightness signature of open water. Flat calm water is very dim to radar, but with wind roughening on a scale comparable to the signal wavelength, it can be very bright. Therefore, under some circumstances which are not easily identifiable, rough water can look like different classes of sea ice. The second problem arises from the fact that radar returns can also be strongly affected by differences in the dielectric properties of the scattering surface. In summer conditions there can be wet snow or melt ponds on top of the ice and this variable water content makes a significant change in the dielectric constant of the material. This can also create enough variation in brightness, not due to ice type, to confuse the classification algorithm.

Given these caveats, the user may interpret the ice classification output product where the different ice types are false colored according to the segmentation and type assignment. By comparing this image with the original SAR image, a knowledgeable analyst can often detect false classifications by identifying leads, ponds or other water phenomena from morphology, structure, texture, etc.

5.3 *OCEAN WAVE SPECTRA*

Ocean waves, because of their roughness and slope, can produce prominent periodic patterns in SAR images. The GPS spatial spectral analysis module processes subsets of a full resolution scene. Each 512×512 block selected by the user is Fourier transformed with a two-dimensional FFT. The transformed wave number spectrum is smoothed by a Gaussian filter with a user adjustable width. The final output product is a contour plot of the spectrum power in polar coordinates with wave number as radius and wave direction (relative to the image orientation) as angle. Significant peaks are automatically located so that the dominant wavelengths and wavefront angles can be displayed. Full details are presented in Holt *et al.* [1990b].

For geolocated images the angles will be bearings with respect to geographic north, otherwise the track angle must be added. The spectra are also available on digital media for further processing by the user.

Appendix A
Signal Processing and Fourier Transforms

A1 *FOURIER TRANSFORMS*

There are many conventions for placing the proportionality constants (involving π) and phase signs in the definition of the Fourier transform and inverse transform pairs. Mathematicians prefer aesthetic symmetries and so will put the π in the phase or distribute it as a scale factor of $1/\sqrt{2\pi}$ for each transform. Engineers prefer the direct approach and so let all the scaling appear in the inverse. Thus,

$$\hat{f}(\omega) := \mathcal{F}\{f\} := \int_{-\infty}^{\infty} f(t)e^{-i\omega t}\,dt, \tag{A1}$$

$$f(t) = \mathcal{F}^{-1}\{\hat{f}\} := \frac{1}{2\pi}\int_{-\infty}^{\infty} \hat{f}(\omega)e^{i\omega t}\,d\omega. \tag{A2}$$

A1.1 *Antenna Power*

To compute the energy pattern as the Fourier transform of the uniform current density across a rectangular antenna, we need to transform the *Heaviside* (also *boxcar* or *rectangle*) function of length D,

$$H_D(x) := \begin{cases} 1 & \text{if } |x| \le D/2, \\ 0 & \text{if } |x| > D/2. \end{cases} \tag{A3}$$

Then

$$\mathcal{F}\{H_D\} = \int_{-D/2}^{D/2} e^{-i\kappa x}\,dx = \frac{e^{i\kappa D/2} - e^{-i\kappa D/2}}{i\kappa} = \frac{2\sin\frac{D}{2}\kappa}{\kappa}. \tag{A4}$$

To get energy density divide by D and square,

$$E = \left(\frac{\sin\frac{D}{2}\kappa}{\frac{D}{2}\kappa}\right)^2 = \operatorname{sinc}^2\frac{D}{2}\kappa = \operatorname{sinc}^2\frac{\pi D\sin\phi}{\lambda}, \tag{A5}$$

where we use the geometric representation of the wave number $\kappa = \frac{2\pi}{\lambda}\sin\phi$ in terms of the off-center beam angle ϕ. Since $\phi < 5^\circ$ we use the small angle approximation to obtain finally

$$E = \operatorname{sinc}^2 \pi\frac{D}{\lambda}\phi. \tag{A6}$$

A1.2 *Complex Gaussian (Chirp)*

The function in this case is $g(t) := e^{-\alpha t^2/2}$ where α may be imaginary. Then

$$\hat{g}(\omega) = \int_{-\infty}^{\infty} e^{-\alpha t^2/2}e^{-i\omega t}\,dt = \int_{-\infty}^{\infty} e^{-\alpha t^2/2 - i\omega t}\,dt. \tag{A7}$$

Let $u = t\sqrt{\alpha/2} + i\omega/\sqrt{2\alpha}$ so that u^2 completes the square of the phase with the term $-\omega^2/2\alpha$ and

$$\hat{g}(\omega) = \int_{-\infty}^{\infty} e^{-u^2-\omega^2/2\alpha}\, dt = \sqrt{\frac{2}{\alpha}} e^{-\frac{1}{\alpha}\omega^2/2} \int_{-\infty}^{\infty} e^{-u^2}\, du = \sqrt{\frac{2\pi}{\alpha}} e^{-\frac{1}{\alpha}\omega^2/2} = \sqrt{\frac{2\pi}{\alpha}} g(\frac{\omega}{\alpha}), \tag{A8}$$

i.e., the transform is a Gaussian scaled by $\sqrt{2\pi/\alpha}$ and frequency scaled by $1/\alpha$.

For the case of the SAR chirp the phase also contains a linear term and the frequency is expressed in cycles so that we need to transform

$$f(t) = e^{i2\pi(f_0 t + at^2/2)} = e^{i2\pi f_0 t} e^{i\pi a t^2}. \tag{A9}$$

This fits Formula (A8) if we choose $\alpha = -i2\pi a$ and apply the Shifting Theorem,

$$\mathcal{F}\{g(t)e^{-ibt}\} = \hat{g}(\omega + b), \tag{A10}$$

with $b = -2\pi f_0$. Thus we have finally

$$\begin{aligned} \hat{f}(\omega) =& \frac{1}{\sqrt{-ia}} \exp\Big(\frac{1}{i2\pi a}(\omega - 2\pi f_0)^2/2\Big) \\ =& \frac{1}{\sqrt{a}} e^{i\pi/4} \exp -i2\pi(f - f_0)^2/2a \\ =& \frac{1}{\sqrt{a}} \exp -i\pi\Big((f - f_0)^2/a - \frac{1}{4}\Big), \end{aligned} \tag{A11}$$

as the Fourier transform of the chirp. Here we have used $\omega = 2\pi f$ (abusing notation on f) and $1/\sqrt{-i} = e^{i\pi/4}$. Then, according to Equation (11) of Section 2.1.2, the reference function for matched filtering of the chirp echo will be the complex conjugate of (A10), i.e.,

$$\hat{f}^*(f) = \frac{1}{\sqrt{a}} e^{i\pi\left((f-f_0)^2/a - 1/4\right)}. \tag{A12}$$

Since, however, the SAR chirp is actually of finite duration T, its signal form is

$$H_T(t - T/2) f(t), \tag{A13}$$

and the reference function is obtained by convolving (A12) with the conjugate of the transform of (A13),

$$\{i(e^{-2\pi i f T} - 1)/2\pi f\} * \hat{f}^*(f), \tag{A14}$$

where the variable of convolution is f. Here we have appealed to the Convolution Theorem (Equation (10) in Section 2.1.2). The convolution can be performed explicitly to get an expression involving a chirp in $f - f_0$ modulated by a Fresnel integral also

varying with $f - f_0$. Simulation has shown that the latter expression can be well approximated by a rectangular window modifying the chirp. Thus the final form for the reference function is

$$H_{aT}(f - f_0)e^{i\pi(f-f_0)^2/a}, \tag{A15}$$

where amplitude and phase have been normalized for simplicity. These quantities are adjusted in the output image by empirical calibration.

A2 *STATIONARY PHASE*

It is apparent that the explicit computation of Fourier transforms may be very difficult or complex. Therefore, it is important to be able to approximate the transforms, given assumptions about the signal waveform. One such technique is the principle of stationary phase [Curlander and McDonough, Ch. 3.2.2, 1991] whereby it is assumed that the phase in the integrand of the transform integral changes slowly with respect to the amplitude at certain times. At other times the phase varies relatively rapidly so that positive and negative contributions to the integral cancel out. Thus only times of stationary phase will contribute significantly to the transform.

It turns out that chirp signals of large time-bandwidth product aT^2 have a unique time of stationary phase given by

$$t_f = (f - f_0)/a. \tag{A16}$$

Thus only portions of the signal near t_f contribute significantly to the transform at frequency f. This fact establishes a linear relationship between time and frequency for such signals. Thus an error in the frequency of the spectrum and/or the reference function of an amount Δf is equivalent to a time shift of the signal by $\Delta f/a$.

For range processing, this amounts to a shift of the image in slant range by

$$c\Delta t/2 = \frac{c}{2a}\Delta f_0 = 9.7\Delta f_0 \text{ meter}, \tag{A17}$$

which is not significant as the variation in carrier frequency f_0 in the signal echo is much less than 1 Hz over the brief duration of the pulse. For azimuth processing an error Δf_D in the Doppler centroid amounts to a time shift in the along track direction of $\Delta f_D/f_R$ and so an azimuth shift of

$$V\Delta f_D/f_R = -\frac{\lambda R}{2V}\Delta f_D = 3.6\Delta f_D \text{ meter}, \tag{A18}$$

using $f_R = -2V^2/\lambda R$. Thus a Doppler error of 3 or 4 Hz will shift the image by a pixel in the azimuth direction. Fortunately, this effect is easily corrected geometrically (Ch. 4).

Appendix B
SAR Doppler Shift

Using the method of T. P. Gill [1965, Ch. I, p. vii], we compute the "change in apparent time interval between two events which arises from the motion of an observer together with the finite velocity of transmission of information."

For SAR we have the configuration shown in Figure A1, where the spacecraft is at S at time t and at S′ at a later time t'. Its speed is V, the time origin is at the point of closest approach to the target T where the spacecraft velocity is perpendicular to the $\overline{\mathrm{ST}}$ vector. The slant range distance from SAR to target is R and the transmission is at light speed c. Our object is to find the change in a small time interval Δt, say the period of a harmonic signal emitted at time t, due to its transmission from S to T and back to the source at S′ at which time its duration is $\Delta t'$.

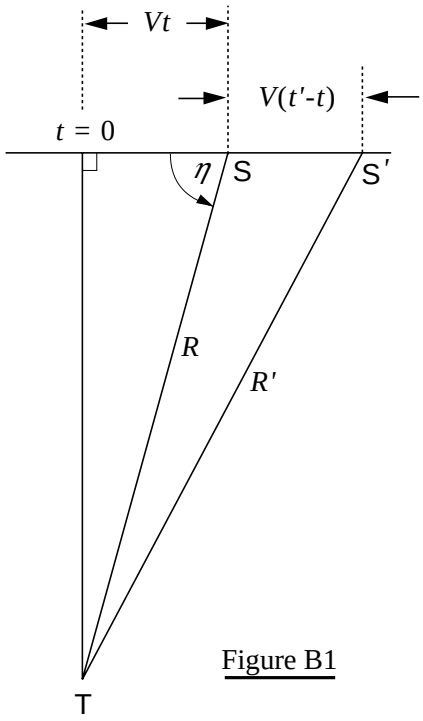

Figure B1

From the geometry of Figure B1 we have

$$\overline{\mathrm{SS'}} = V(t' - t), \tag{B1}$$

$$R + R' = c(t' - t), \tag{B2}$$

$$R\cos\eta = Vt, \tag{B3}$$

and from the law of cosines

$$R'^2 = V^2(t' - t)^2 + R^2 + 2RV(t' - t)\cos\eta. \tag{B4}$$

Substituting for R' from (B2) and solving for $t' - t$ gives

$$t' - t = \frac{2}{c^2 - V^2}(Rc + RV\cos\eta). \tag{B5}$$

Applying (B3) this becomes

$$t' = t + \frac{2}{c^2 - V^2}(Rc + V^2 t). \tag{B6}$$

Differentiate with respect to t to get

$$\frac{dt'}{dt} = 1 + \frac{2}{c^2 - V^2}(\dot{R}c + V^2). \tag{B7}$$

Approximating with small time intervals Δt and $\Delta t'$ produces finally

$$\Delta t' = \Delta t\big(1 + \frac{2}{c^2 - V^2}(\dot{R}c + V^2)\big). \tag{B8}$$

So far we have made an approximation of straight line travel of S instead of the curved orbital flight path. To estimate numerical values we use ERS-1 parameters. Thus for an integration time of 0.6 sec and orbit period of 6028 sec this is an error on the order of the small angle approximation for an angle of $.6 \times 2\pi/6028 = .00063$rad. This relative error is about 7×10^{-8}. By the Mean Value Theorem the differential approximation introduces a relative error of no more than $2V^2\Delta t/Rc = 2V^2\lambda/Rc^2 = 8 \times 10^{-17}$ which is entirely neglible.

To get from (B8) to the standard formula,

$$\Delta t' = \Delta t(1 + \frac{2}{c}\dot{R}), \tag{B9}$$

we neglect V^2 with respect to $\dot{R}c$ and replace $c/(c^2 - V^2)$ with $1/c$. Then reciprocating (B9) transforms from period to frequency to give

$$\begin{aligned} f' &= f(1 + \frac{2}{c}\dot{R})^{-1} \\ &\approx f(1 - \frac{2}{c}\dot{R}). \end{aligned} \tag{B10}$$

The approximation in (B10) has a relative error of $(2\dot{R}/c)^2 = (2V^2t/Rc)^2 \leq 2 \times 10^{-13}$ (where we use $\dot{R} = V^2t/R$), again neglible. Finally we obtain the Doppler shift,

$$f_D = f' - f = -\frac{2f}{c}\dot{R} = -\frac{2}{\lambda}\dot{R}. \tag{B11}$$

The errors examined so far are cumulatively less than 1 in 10^7. It remains to evaluate the difference between (B8) and (B9) as it affects f_D, i.e., the error between $2(\dot{R}c + V^2)/(c^2 - V^2)$ and $2\dot{R}/c$. This is

$$\frac{2V^2}{c^2 - V^2}\left(1 + \frac{\dot{R}}{c}\right) \approx 2\left(\frac{V}{c}\right)^2 = 1.24 \times 10^{-9}. \tag{B12}$$

This small relativistic time shift amounts to a nearly constant error of about 6.6 Hz at the ERS-1 signal frequency of 5.3 GHz. Thus at $t = 0$ the true Doppler shift will be -6.6 rather than zero. The true Doppler centroid will occur at $\dot{R}c = V^2$, i.e., at $t = R/c$, where we have again used $\dot{R} = V^2t/R$. For ERS-1 this is about .0028 sec which implies an along track shift of about 19 m or 1 to 2 pixels in azimuth. At maximum doppler the relative error will be about .3%.

A final approximation occurs because the signal is not a pure harmonic. The ERS-1 output pulse is a chirp (linear FM) with a bandwidth of 15.5 MHz. Since f_D is directly proportional to frequency, the relative error due to frequency variation will be 15.5 MHz/5.3 GHz=.0029, or again .3% error. Thus $\Delta f_D = .003 f_D$ throughout the Doppler bandwidth as opposed to the relativistic error which is a constant 6.6 Hz.

Appendix C
Mission and Product Descriptions

	Mission		
Orbit	ERS-1	JERS-1	Radarsat
Altitude	785 km	568 km	793-821 km
Inclination	98.516º	97.662º	98.594º
Period	6027.907 s	5799.72 s	6042 s
Repeat Cycle	3**,** (35, 176) days	44 days	24 days
Orbit Type	sun synchronous	sun synchronous	sun synchronous
Ground Track Velocity	6.628 km/s	6.883 km/s	6.576 km/s
Instrument			
Frequency	C-Band (5.3 GHz)	L-Band (1.275 GHz)	C-Band (5.3 GHz)
Wavelength	5.66 cm	23.5 cm	5.66 cm
Pulse Repeition Freq.	1640–1720 Hz	1505.8–1606 Hz	1270–1390 Hz
Pulse Length (BW)	37.1 μs (15.5 MHz)	35 μs (15 MHz)	42 μs (11.6,17.3,30 MHz)
Polarization	VV	HH	HH
Antenna Size L x W	10 X 1 m	11.9 X 2.4 m	15 X 1.5 m
Peak Power	4.8 kW	1.3 kW	5 kW
Average Power	300 W	71 W	300 W
Noise Equivalent σ_0	-18 dB	-20.5 dB	-21 dB
Image			
Swath Width	100 km	75 km	50,100,150,500 km
Max Resolution Rg x Az	12.5 X 12.5 m	7 X 7 m	10 X 10 m
Resolution @ # looks	30 @ 4	18 @ 3	28 X 30 @ 4
System			
On Board Storage	None	Tape 20 min	2 Tapes @ 14.5 min
Look Angle	Right 20.355º	Right 35.21º	R & L 20–50º
Incidence Angles, Mid	19.35–26.50º, 23º	36.14–41.51º, 38.91º	22.64–59.56º, 45.12º
Footprint Rg x Az	80 X 4.8 km	70 X 14 km	50-150 X 4.3 km
Doppler BW	1260 Hz	1157 Hz	939 Hz
Coherent Integ Time	.6 s	1.7 s	.46 s
Windowing	Hamming	Hamming	Hamming
Pulse Compression Ratio	580:1	525:1	491, 727, 1260:1
Range Sample Rate	18.96 MHz	17.1 MHz	12.9, 18.5, 32.3 MHz
Maximum Data Rate	105 Mb/s	30 Mb X 2 Mb/s	105 Mb/s
Quantization	5 bits/sample	3 bits/sample	4 bits/sample

Table C1. The orbit parameters for ERS-1 are for the 3-day repeat cycle. They will be slightly different for the 35- and 176-day orbit cycles. Sources of the data are various. Some are estimates, some are specifications, some are calculated, some are operational, and some even are measurements.

ASF SAR Imagery and Derived Products

Level	Product Name	Processing & System	Data Type (samples)	Bit Quantization or Units	# Lines	# Samples	Pixel Spacing (meters)	Resolution (meters)	Extent
0	Computer Compatible Signal Data	Raw Video Signal RGS	Complex	5I X 5Q	NA	NA	NA	NA	12 sec
1A	Complex Image	One-look SAR Processed SPS	Complex	16I X 16Q	6250	3750	8	10	30 X 50 km
1B	Full Resolution Image	Four-look SAR Processed SPS	Integer	8	8192	8192	12.5	30	100 X 100 km
1B	Low Resolution Image	256-look (8 X 8 avg) SAR Processed SPS	Integer	8	1024	1024	100	240	100 X 100 km
1B	Geocoded Full Resolution Image	Geolocated Four-look AOS	Integer	8	8192	8192	12.5	30	100 X 100 km
1B	Geocoded Low Resolution Image	Geolocated 256-look AOS	Integer	8	1024	1024	100	240	100 X 100 km
2	Ice Type Classification	Segmented into 3 or 4 Classes GPS	Integer	4	1024	1024	100	240	100 X 100 km
2	Ocean Wave Spectra	2D PS Contour Plot Wavelength & Dir GPS	Real	meters, degrees	17	17	6000	6000	100 X 100 km
3	Ice Type Fraction	3 or 4 Band Concentration of Ice Type GPS	Real	%	20	20	5000	5000	100 X 100 km
3	Ice Motion Vectors	$(\Delta x, \Delta y)$, Displacement GPS	Real	km	20	20	5000	5000	100 X 100 km

Table C2. Products available for ordering by investigators at ASF. The level (Col. 1) is a technical designation specifying the stages of processing involved in production. Level definitions are provided in Curlander and McDonough [1991, Table 6.1]. Processor descriptions can be found in the various JPL documents listed in the Bibliography. Complex data samples have integer real part I (*Inphase*) and integer complex part Q (*Quadrature*). The pixel spacing represents the size of the element on the ground for which the DN value applies. The resolution, when larger, applies to the ability of the instrument/signal processing system to spatially differentiate returns from the imaged surface. All products are available on computer compatible magnetic tape (CCT) and 5.25" digital optical disks (DOD). All level 1B data is also available on 8 X 10" film transparencies or prints in either black and white photo or dry silver (Lasertechnics).

Appendix D
Side Looking Radar Swath Geometry

In Figure D1 a SAR S flies at altitude H above a spherical earth of radius R_e and center C. It looks to the side at angle θ toward target T which is on the surface at slant range R and ground range r. Let ρ be the angle between S and T subtended at C and φ be the incidence angle of the beam at the target.

Elementary trigonometry gives us the following relationships:

$$r = \rho R_e \tag{D1}$$

$$\varphi = \rho + \theta \tag{D2}$$

$$\sin\varphi = \frac{R_e + H}{R_e}\sin\theta \tag{D3}$$

$$\cos\theta = \frac{R^2 + 2HR_e + H^2}{2R(R_e + H)} \tag{D4}$$

$$R^2 = 2R_e(R_e + H)(1 - \cos\rho) + H^2. \tag{D5}$$

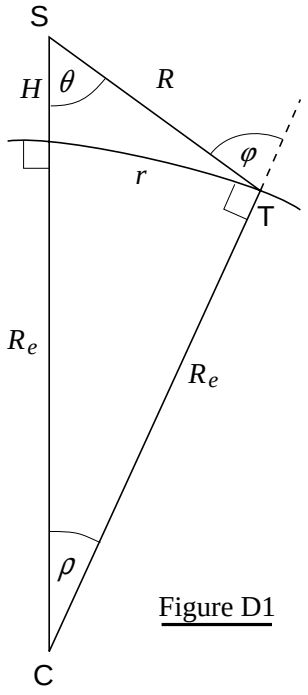

Figure D1

Now given R_e, H, mid-swath look angle θ and swath width W, we can solve for the remaining four unknowns of the mid-swath case by using (D3) to find φ, (D2) to find ρ, (D1) to find r and (D5) to find R. For the near and far swath edge cases, compute ground range as $r \pm W/2$. Then find ρ from (D1), R from (D5) θ from (D4) and φ from (D2).

To find the variation of r with R, differentiate (D5) with respect to r and note that $d\rho/dr = 1/R_e$,

$$R\frac{dR}{dr} = (R_e + H)\sin\rho. \tag{D6}$$

Using the law of sines for ρ and θ and reciprocating gives

$$\frac{dr}{dR} = \frac{R_e}{(R_e + H)\sin\theta}, \tag{D7}$$

which is the formula referenced in Section 4.2.

To obtain spherical earth formulas for determining the occurrence of layover and shadowing corresponding to (39) and (41) in section 4.2.1, we need to find dR/dr and $d\varphi/dr$ from the geometry of Figure D1, but with distance $\overline{CT}$ given by $R_e + h(r)$. Then write the law of cosines for ρ and differentiate with respect to r to get

$$R\frac{dR}{dr} = \big((R_e + h) - (R_e + H)\cos\rho\big)\frac{dh}{dr} + \frac{(R_e + H)(R_e + h)}{R_e}\sin\rho. \tag{D8}$$

Similarly, differentiating the law of cosines for φ yields

$$\frac{d\varphi}{dr} = \frac{(R + (R_e + h)\cos\varphi)\frac{dR}{dr} + (R_e + h + R\cos\varphi)\frac{dh}{dr}}{R(R_e + h)\sin\varphi}. \tag{D9}$$

Here we can use the value of dR/dr from Equation (D8).

It is clear that these expressions are considerably more complex than (39) and (41) of Section 4.2.1. Thus, given that the accuracy and resolution of the DEM is such that the estimate for the local slope dh/dr will contain greater error than the flat earth approximation, it is more efficient to use the simpler expressions.

Using the algorithm of (D1)–(D5) and values for H, θ, and W from Table C1, and an R_e at latitude of the ASF (64.86°N), produces the following table.

ERS–1	ρ	r	θ	φ	R
	(deg)	(km)	(deg)	(deg)	(km)
Near Edge	2.197	243.9	17.157	19.354	826.5
Mid Swath	2.647	293.9	20.355	23.002	844.5
Far Edge	3.098	343.9	23.398	26.496	865.5
JERS–1					
Near Edge	3.360	373.0	32.775	36.135	688.5
Mid Swath	3.698	410.5	35.210	38.908	711.4
Far Edge	4.036	448.0	37.478	41.514	735.6
Radarsat					
Near Edge	2.640	293.0	20.000	22.640	856.4
Mid Swath	6.100	677.1	39.019	45.119	1073.5
Far Edge	9.560	1061.2	50.000	59.560	1378.9

Table D1. Swath parameters for three SARs

Glossary and Definition of Acronyms

active
: In *layover* and *shadowing*, referring to regions subject to terrain distortion because of their orientation with respect to the radar beam.

aliasing
: Folding of higher into lower frequency components in a discrete spectrum due to undersampling of the signal.

ambiguity
: In *pulse compression*, the leakage of sidelobe energy into adjacent pixels. In *azimuth processing*, recurrence of bright targets at multiples of the PRF. See *ghost* and *aliasing*.

ambiguity function
: A generalized signal autocorrelation measuring the resolution due to *pulse compression*.

AOS
: Archive and Operating System. The overall ASF data management system.

ascending pass
: South to north trending relative earth orbit motion of a satellite.

ASF
: Alaska SAR Facility.

ASP
: Alaska SAR Processor.

autofocus
: In SAR processing, a data dependent method for determining the Doppler rate f_R.

azimuth
: The horizontal direction in radar sensing. In SAR, the along track direction.

backscatter
: Radar signal energy scattered back toward the instrument.

BW
: BandWidth. The frequency range contained in a signal or passed by a filter.

carrier
: The base frequency of the radar output which is modulated by the signal waveform.

CCT
: Computer Compatible Tape. Half inch magnetic digital tape, usually recorded at 1600 or 6250 bytes per inch (BPI).

chirp
: A *linear FM* waveform used for the outgoing radar pulse.

clutter
: Random background noise in a radar image due to scattering from a surface with homogeneous roughness on a scale larger than the signal wavelength.

clutterlock
: In SAR processing a data dependent method for determining the Doppler shift f_D.

coherent integration time
: In SAR processing, the period over which azimuth information is integrated. The time interval during which the target is in the radar beam and phase coherent information is collected for integration.

composite
: An image composed pixel by pixel from two or more component images according to a selection procedure.

corner reflector
: A trihedral target made from aluminum screen and oriented on the ground toward the radar to provide a bright pixel for image intensity calibration.

correlator
: A synonym for the SAR processor referring to the equivalence of its procedure to cross-correlation. See *matched filter*.

cosine on a pedestal
: A *window* or frequency weighting function of the form $\alpha + \beta \cos(2\pi f)$.

DEM
: Digital Elevation Model. Terrain height data given on a regular map grid.

descending pass
: North to south trending relative earth orbit motion of a satellite.

deskew
: In SAR processing, a resampling procedure designed to remove skew from the processed image due to minor geometric errors such as earth eccentricity.

DLR
: Deutsche Forschungsanstalt für Luft- und Raumfahrt e. V. (German Aerospace Research Establishment).

DN
: Data Number or (redundantly) Digital Number. The intensity value assigned to a pixel in an image, usually an integer scaled to one byte (0 – 255) and not having any physical or engineering units associated with it.

DOD
: Digital Optical Disk. Read-only 5.25" optical media for image storage and transport.

Doppler centroid
: The center Doppler frequency or null of the Doppler spectrum as the radar beam sweeps past the target. Designated f_D.

Doppler history
: The Doppler centroid and its time rate of change. These parameters are used to compute the azimuth processing *reference function*.

EDC
: EROS Data Center. Earth remote sensing data center for USGS in Sioux Falls, South Dakota.

EROS
: Earth Resource Observation System. See *EDC*.

ERS-1
: Earth Resource Satellite. The ESA satellite launched in summer 1991 carrying, among others, a SAR instrument.

ESA
: European Space Agency.

feathering
: In *mosaicking*, a blending technique to reduce discontinuities at seams between component images.

FFT
: Fast Fourier Transform. An efficient algorithm for computing the discrete Fourier transform of a discrete signal. Used in harmonic or spectral analysis.

flattening
: 1− ratio of polar to equatorial radii of the earth. A measure of the eccentricity, $e = \sqrt{2f - f^2}$.

FM
: Freqency Modulation, as of a *carrier* wave.

footprint
: The area on the ground intersected by the radar beam.

foreshortening
: In terrain correction, the apparent spatial compression in the image of slopes facing the radar.

frequency response function
: The fourier transform of the *impulse response function*.

GEI
: Geocentric Equatorial Inertial, a rectangular coordinate system.

geocentric equatorial inertial
: The rectangular space fixed earth coordinate system used for *geolocation*.

geocoding
: Geometric correction and registration of an image to map coordinates, often involving terrain correction for SAR images.

geoid
: An ellipsoid of rotation earth model.

geolocation
: The mathematical correspondence between image coordinates (line, sample) and geographic coordinates (lat, long).

ghost
: An image of a bright target repeated at azimuth intervals due to spatial *ambiguity* corresponding to sidelobe aliasing of the along track antenna pattern at distances corresponding to multiples of the *PRF*.

global incidence angle
: The angle of the radar beam center from the normal to the geoid surface at the target.

GPS
: Geophysical Processor System. Note that this is *not* the prior and much more widely known satellite navigation system, Global Positioning System.

ground range
: The distance along the surface from the *nadir* point to the target.

ground truth
: Observations near the surface relating phenomena to corresponding features in a remotely sensed image.

Hamming window
: A form of the *cosine on a pedestal* weighting function where $\alpha = .54$ and $\beta = .46$.

impulse response function
: The characteristic function of a linear time-invariant filter, which, convolved with the input signal, produces the output. If input is a δ function, output is the impulse response function.

inclination
: The angle of the plane of a satellite orbit with respect to the equatorial plane of the earth. An inclination of 90° gives a polar orbit.

in-phase
: Engineering term for the real part of a complex signal.

inter-pulse period
: The time interval between successive radar transmission pulse beginnings. See *IPP*.

IPP
: Inter-pulse period. IPP = 1/PRF.

JERS-1
: The Japenese Earth Resources Satellite launched by NASDA in December of 1991 and also carrying a SAR instrument. See Appendix C, Table C1.

JPL
: Jet Propulsion Laboratory. Site of the major development of ASF systems. A NASA installation for unmanned space exploration managed by California Institute of Technology in Pasadena, California.

layover
: In terrain correction, the apparent reversal in range sequence and overlapping onto adjacent range intervals of images of slopes facing the radar at angles steeper than the *global incidence angle*.

linear frequency modulation
: A phase coded pulse modulation of the carrier frequency, e.g., $\cos((\omega_0 + \omega t)t)$, $t_1 \leq t \leq t_2$.

local incidence angle
: The angle between the radar beam center and the normal to the local topography. The difference between the *global incidence angle* and the *terrain slope*.

look
: In SAR processing, an image processed with a fraction of the reference spectrum (chirp or Doppler) resulting in multiple images at reduced resolution.

look angle
: Of a SAR, the angle up from the nadir at which the radar beam is pointed. Of a target, the angle between the SAR-nadir and SAR-target lines.

matched filter
: A filter designed to compress a known signal into a short pulse. Equivalent to pulse compression by cross-correlation with the time reversed conjugate of the expected waveform.

mosaicking
: A strange word referring to the assembling of a number of similar parts into a larger whole. Specifically, the merging of overlapping images of adjacent terrain into a scene covering the entire area.

nadir track
: The path on the surface directly below the flight path of the instrument.

NASA
: National Aeronautics and Space Administration (of the United States).

NASDA
: National Aeronautics and Space Development Agency (of Japan).

passive
: In terrain correction, referring to areas of topography that are *laid over* or *shadowed* by *active* areas.

polarization
: The orientation of the electromagnetic vector of the transmitted radar signal.

PRF
: Pulse Repetition Frequency.

pulse compression ratio
: The duration of the transmitted pulse divided by the duration of the compressed pulse.

pulse repetition frequency
: The repetition rate of the outgoing radar pulses.

quadrature
: Engineering term for the imaginary part of a complex signal.

quantization
: Engineering term for number of bits per sample of a digitized signal.

range
: The distance direction for a radar. In SAR, the cross track direction.

range curvature
: In SAR processing, the nonlinear path in pixel coordinate space of the returns from a target due to variation of the distance between radar and target as the beam passes over the target. Azimuth integration must be done over this path.

range migration
: The combination of *range walk* and *range curvature*.

range walk
: The contribution to the nonlinear path in pixel space due to the Doppler variation from earth rotation relative motion.

reference function
: The *frequency response function* used for frequency domain filtering in azimuth and range SAR processing. In the time domain, the *impulse response function*.

resolution
: The ability of the radar and processing system to discriminate between targets on the ground.

RGS
: Receiving Ground Station. The antenna and demodulating stage of the SAR data downlink.

SAR
: Synthetic Aperture Radar.

shadow
: Areas in the image where steep terrain blocks the radar beam. Only noise values appear in these pixels.

sifting
: The convolutive identity property of the δ function.

slant range
: The distance from radar to target.

SMMR
: Scanning Multichannel Microwave Radiometer. A NASA passive microwave remote sensing satellite.

SNR
: Signal to Noise Ratio.

sophisticated
: Signals (particularly radar pulses) with high time-bandwidth product.

speckle
: Spatially random multiplicative noise due to coherent superposition of multiple backscatter sources within a SAR resolution element.

SPOT
: System Probatoire d'Observation de la Terre. French optical band remote sensing satellite.

SPS
: SAR Processor System. The guts of the ASF computer systems.

squint angle
: The angle between the radar beam center and the normal to the flight path.

STALO
: STAble Local Oscillator. The high precision on-board clock which enables phase control in SAR processing.

stationary phase
: An approximately direct time-frequency relationship for spectral analysis of *sophisticated*, e.g., *chirp* signals.

sun synchronous
: An earth satellite near polar orbit which has a period of revolution and orbit precession which keep the plane of the orbit fixed with respect to the sun-earth line. If the intersection with the equatorial plane is perpendicular to the sun-earth line, it is called a *dawn–dusk* orbit which maximizes solar exposure of the photoelectric power panels.

swath
: The strip of ground swept over by the moving radar beam.

terrain slope
: The angle between the local tangent to the surface and the horizontal.

tiepoint
: A recognizable feature on the surface which can be related geographically to an image or between images.

USGS
: United States Geological Survey.

vernal equinox
: The direction in space along the sun-earth line when the earth axis is perpendicular to the sun-earth line and the north pole is inclined away from the direction of the earth orbital velocity.

window
: A finite duration weighting function, commonly of unit energy, which is multiplied against a signal for the purpose of improving the spectrum by removing high frequency components due to truncation in time.

List of Symbols and Definitions

a	Chirp frequency rate.
acf	Autocorrelation function.
$\mathbf{A}_{\text{S}}$	SAR acceleration vector.
$\mathbf{A}_{\text{T}}$	Target acceleration vector.
B	Bandwidth
c	Light speed.
D	Antenna height.
e	Eccentricity of an ellipse (geoid or orbit).
E	Energy of a signal.
f	As a function name, a generic complex signal.
	As an argument, a generic frequency in Hz.
	As a parameter, geoid flattening factor, ($:= (R_E - R_P)/R_E = 1/298.255$).
$\mathcal{F}$	Fourier transform operator.
f_0	Radar carrier signal frequency.
f_D	Doppler frequency shift.
f_R	Doppler rate ($:= \dot{f}_D$).
f_s	Range sampling rate.
g, s	Generic complex output signal.
h	As a function name, generic complex impulse response function.
	As a parameter, target elevation above geoid (sea level).
H	SAR orbit altitude above earth.
H_D	Heaviside (boxcar, rectangle) function of width D.
i	Imaginary unit ($:= \sqrt{-1}$).
(i, j)	Slant range image pixel numbers.
L	Antenna length.
$\overline{P}$	Average transmitter power.
(p, q)	Geocoded map grid image pixel numbers.
$P_\oplus$	Sidereal earth day, 23.93447 hr.
r	Ground range.
R	Slant range.
R_0	Minimum slant range.
R_E	Earth equatorial radius.
R_e	Earth radius.
R_P	Earth polar radius.
(r, s)	Natural image coordinates.
$\mathbf{R}_{ij}$	Target to SAR position vector.
$\mathbf{R}_{\text{S}}$	SAR position vector.
$\mathbf{R}_{\text{T}}$	Target position vector.
t	Time.
T	Radar pulse duration.
t_f	Time of stationary phase.
$\mathbf{u}$	Unit normal vector to geoid.

V	Speed of SAR sensor in orbit path.
v_e	Earth sidereal surface centriputal speed.
$\mathbf{V}_{\mathrm{S}}$	SAR velocity vector.
$\mathbf{V}_{\mathrm{T}}$	Target velocity vector.
(X, Y)	Map coordinates.
(x, y, z)	Rectangular coordinates (GEI).
$(x_{\mathrm{S}}, y_{\mathrm{S}}, z_{\mathrm{S}})$	GEI coordinates of the SAR.
$(x_{\mathrm{T}}, y_{\mathrm{T}}, z_{\mathrm{T}})$	GEI coordinates of the target.
α	Terrain slope angle.
α_i	Scattering intensity at range sample $i\Delta t$.
β	Bearing of nadir track with respect to north.
γ	Radar beamwidth angle.
δ	Dirac delta (unit impulse) function.
Δ	Difference operator.
δt	Time correction in Newton's method.
Δt	Signal sampling time interval.
(ζ, χ)	Geodetic latitude, longitude.
θ	Look angle.
κ	Wave number.
λ	Radar carrier signal wavelength.
Λ	Layover indicator function.
π	3.14159 26535
ρ	Central angle at earth center between SAR and target.
ρ_r	Range resolution.
ρ_z	Azimuth resolution.
σ	Radar scattering cross section of a target.
Σ	Shadowing indicator function.
σ^0	Target radar backscatter coefficient.
τ	Lag time.
Υ	Aries (The Ram). The vernal equinox.
φ	Radar beam incidence angle.
ϕ	Off-center radar beam angle.
Φ	Radar carrier signal harmonic.
φ_{T}	Local incidence angle ($:= \varphi - \alpha$).
χ^2	Chi-squared probability distribution
ω	Generic circular frequency in rad/sec.
ω_e	Earth sidereal angular speed, 7.2292115×10^{-5} rad/sec.
$\overrightarrow{\omega_e}$	Earth sidereal angular velocity vector.
§	Section of a document.

Bibliography and References

Bracewell, R. N., *The Fourier Transform and Its Applications*, McGraw-Hill, New York, 1965.

Curlander, J. C. and R. N. McDonough, *Synthetic Aperture Radar, Systems and Signal Processing,* John Wiley & Sons, New York, 1991.

Dade, E. F., D. A. Rothrock, R. Colony and C. Olmsted, *Estimating Repeat Coverage of Arctic Sea Ice with ERS-1 SAR,* University of Washington Technical Report APL-UW TR9114, July 1991.

Elachi, C., T. Bicknell, R. L. Jordan, and C. Wu, Spaceborne synthetic-aperture imaging radars: Applications, techniques, and technology, *Proc. IEEE*, v70, p1174-1209, 1982.

Fitch, J. P., *Synthetic Aperture Radar*, Springer-Verlag, New York, 1988.

Gill, T. P., *The Doppler Effect*, Logos Press, 1965.

Harger, R. O., *Synthetic Aperture Radar Systems: Theory and Design*, Academic Press, New York, 1970.

Holt, B., R. Kwok and E. Rignot, Status of the ice classification algorithm in the Alaska SAR Facility Geophysical Processor System, *Proc. IGARSS '90, Washington, DC,* p2221-2224, 1990a.

Holt, B., R. Kwok and J. Shimada, Ocean wave products from the Alaska SAR Facility Geophysical Processor System, *Proc. IGARSS '90, Washington, DC,* p1469-1473, 1990b.

Hovanessian, S. A., *Introduction to Synthetic Array and Imaging Radars*, Artech House Inc., Norwood MA, 1980.

Kovaly, J. J., *Synthetic Aperture Radar*, Artech House Inc., Norwood MA, 1976.

Kropatsch, W. G. and D. Strobl, The generation of SAR layover and shadow maps from digital elevation models, *IEEE Trans. Geosci. and Remote Sensing*, v28, p98-107, 1990.

Kwok, R., J. C. Curlander and S. Pang, Rectification of terrain induced distortions in radar imagery, *Photogrammetric Engineering and Remote Sensing,* v53, p507-513, 1987.

Kwok, R., J. C. Curlander, R. McConnell and S. S. Pang, An ice-motion tracking system for the Alaska SAR Facility Geophysical Processor System, *IEEE J. Ocean Eng.,* v15, p44-54, 1990a.

Kwok, R., J. C. Curlander and S. Pang, An automated system for mosaicking spaceborne SAR Imagery, *Int. J. Remote Sensing,* v11, p209-223, 1990b.

Rignot, E.J.M., R. Kwok, J. C. Curlander and S. S. Pang, Automated multisensor registration: Requirements and techniques, *Photogrammetric Engineering and Remote Sensing,* v57, p1029-1038, 1991.

Roth, A., H. Craubner and Th. Bayer, Prototype SAR geocoding algorithms for ERS-1 and SIR-C/X-SAR images, *Proc. IGARSS '89* (Vancouver, Canada), v2, p604-607, 1989.

Schreier, G., D. Kosmann, and A. Roth, Design aspects and implementation of a system for geocoding satellite SAR-images, *ISPRS J. Photogram. and Remote Sensing,* v45, p1-16, 1990.

Skolnik, M. I., Ed., *Radar Handbook*, McGraw-Hill, New York, 1990.

Ulaby, F. T., R. K. Moore and A. K. Fung, *Microwave Remote Sensing,* v III, Artech House Inc., Norwood MA, 1986.

Vakman, D. E., *Sophisticated Signals and the Uncertainty Principle in Radar*, Springer-Verlag, New York, 1968.

Walker, J. L., Range-Doppler imaging of rotating objects, *IEEE TAES*, v16, p23-52, 1980.

Wivell, C. E., D. R. Steinwand, D. J.Meyer and G. G. Kelly, The evaluation of digital elevation models for geocoding synthetic aperture radar images, *IEEE Trans. Geosci. and Remote Sensing*, in press, 1992.

Wivell, C., C. Olmsted, D. Steinwand and C. Taylor, Spaceborne SAR Image Intensity Corrections by Composition of Opposing Looks, *Proceedings of the Ninth Thematic Conference on Geologic Remote Sensing: Exploration, Environment, and Engineering, 8-11 February 1993, Pasadena, California,* Environmental Research Institute of Michigan, Ann Arbor, Michigan, 1992

Jet Propulsion Laboratory Documents,

DeSoto, Y., H. Tippens, T. Kotlarek and I. Hsu, *Alaska SAR Facility Archive and Catalog Subsystem User's Guide,* JPL D-5496, March 1991.

Baltzer, T., M. Karspeck, R. McConnell and D. Meyerson, *Alaska SAR Facility Geophysical Processor System User's Guide,* JPL D-7867, July 1991.

Alaska SAR Facility, *SAR Processor System.*

Carande, R. E., K. Leung and K. Vines, *Functional Requirements Document,* JPL D-4052, July 1987.

Carande, R. E., *Functional Design Document,* JPL D-4922, February 1988.

Bicknell, T., *Software Requirements Document,* JPL D-5363, June 1988.

Chu, E., *Post Processor, Software Specifications Document,* JPL D-5364 v1, June 1988.

Carande, R. E., P. Jennex, A. Slutsmeyer, *Alaska SAR Processor, Software Specifications Document,* JPL D-5364 v2, December 1988.

Bicknell, T., *User's Guide to Products,* JPL D-9362, January 1992.

Alaska SAR Processor

Slutsmeyer, A., *Programmers Technical Manual,* Working Document, February 1991.

Robnett, T., *Principles of Operation,* Working Document, 1991.